

Submitted by
Julian Hofer, B.Sc.

Submitted at
Institute of Semiconductor and Solid State Physics

Supervisor
Prof. Dr. Armando Rastelli

Co-Supervisor
DI Christian Schimpf

month year

Exciting and Resolving Quantum Dot Emission with Adiabatic Rapid Passage and Fabry Perot Interferometry



Master Thesis
to obtain the academic degree of
Diplom-Ingenieur
in the Master's Program
Technische Physik

Eidesstattliche Erklärung

Ich erkläre an Eides statt, dass ich die vorliegende Masterarbeit selbstständig und ohne fremde Hilfe verfasst, andere als die angegebenen Quellen und Hilfsmittel nicht benutzt bzw. die wörtlich oder sinngemäß entnommenen Stellen als solche kenntlich gemacht habe. Die vorliegende Masterarbeit ist mit dem elektronisch übermittelten Textdokument identisch.

Datum

Unterschrift

Acknowledgement

First I would like to thank the head of our group Armando Rastelli for offering me this position and for making sure to always have an open ear, no matter how busy he was at the moment. I would also like to thank Christian Schimpf for taking the role as my unofficial supervisor. I can not think of anyone who would have fulfilled it better than him. Thanks belongs to most of my group members but I want to especially highlight Marcus Reindl and Daniel Huber who granted me the biggest support. Further, I would like to thank Susanne Schwind for solving every administrative issue that came along my way.

Last but not least, I would like to thank my parents for supporting every goal I have ever pursued in my life and of course Sabrina for more reasons than I could ever possibly list.¹

¹This document is set in Palatino, compiled with pdfL^AT_EX2e and Biber. The L^AT_EX template from Karl Voit is based on KOMA script and can be found online: <https://github.com/novoid/LaTeX-KOMA-template>

Zusammenfassung

Geräte, die auf Quantentechnologie basieren, sind prädestiniert, Teil unseres täglichen Lebens zu werden. Halbleiterquantenpunkte mit ihren diskreten elektronischen Zuständen sind vielversprechende Kandidaten für dieses Gebiet und ideal für die Erforschung der Quantenoptik. Aus diesem Grund werden in dieser Arbeit zunächst Herstellungsverfahren und optische Eigenschaften von GaAs-Quantenpunkten vorgestellt.

Die weitere Diskussion ist in zwei Kapitel unterteilt, deren gemeinsamer Nenner GaAs-Quantenpunkte sind. Das erste befasst sich mit der resonanten Zwei-Photonen-Anregung mittels "adiabatic rapid passage". Bei diesem Verfahren werden gechirpte Laserpulse verwendet, deren Charakterisierung, Simulation und Messung den größten Teil dieses Kapitels ausfüllen. Der zweite Teil behandelt die spektrale Auflösung der Quantenpunktemission mittels eines Scanning Fabry-Pérot-Interferometers. Hier wird der Leser zunächst durch den Aufbau der mathematischen Beschreibung der Fabry-Pérot-Modi geführt. Anschließend werden Simulationen vorgestellt, mit deren Hilfe die Komponenten des Interferometers dimensioniert werden. Schließlich wird die Feinstruktur des Biexcitons im Rahmen eines Proof-of-Principle-Experiments aufgelöst.

Abstract

Devices based on quantum technology are predestined to be part of our everyday lives. Semiconductor quantum dots with their discrete electronic states are promising candidates for this field and are ideal for research in quantum optics. That is why this thesis starts by introducing fabrication methods and optical properties of droplet-etched GaAs quantum dots.

The further work is splitted in two chapters with GaAs quantum dots as their common denominator. The first one deals with resonant two-photon excitation via adiabatic rapid passage. In this procedure chirped laser pulses are used and their characterization, simulation and measurements will fill the majority of this chapter. The second one investigates the capabilities of resolving quantum dot emission with a scanning Fabry Pérot interferometer. Initially, the reader is guided through the build-up of the mathematical description of the Fabry Pérot modes. Afterwards, simulations will be presented which are used to size the interferometer components. Finally the fine-structure of the biexciton will be resolved in a proof-of-principle experiment.

Contents

Zusammenfassung

Abstract

1. Introduction	1
1.1. Setup	2
2. Droplet etched gallium arsenide quantum dots	3
2.1. Fabrication and optical properties	3
2.2. Fine structure splitting	6
2.3. Zero-phonon line and phonon sideband	6
2.4. Optical excitation of a quantum dot	9
2.5. Single photon emission	11
3. Entangled photon generation using adiabatic rapid passage with frequency-chirped pulses	13
3.1. Introduction and motivation	13
3.2. Chirp	13
3.3. Measuring the chirp with interferometric autocorrelation	15
3.4. Deterministically adjusting the chirp with a pulse expander	16
3.5. Adiabatic rapid passage	17
3.6. Simulation	18
3.7. Measurements and discussion	21
4. Building up a scanning Fabry-Pérot interferometer from scratch	23
4.1. Introduction and motivation	23
4.2. Transverse modes of electromagnetic radiation	23
4.2.1. Gaussian beam	23
4.2.2. Higher Gauss modes	26

4.3.	Fundamentals of Fabry-Pérot interferometers	27
4.3.1.	Resonator losses	27
4.3.2.	Resonance frequencies, free spectral range and spectral line shapes	28
4.3.3.	Airy distribution of Fabry-Pérot interferometers	29
4.3.4.	Airy linewidth and finesse	30
4.3.5.	Mode matching and spatial filtering	32
4.3.6.	Confocal setup	35
4.4.	Simulation	36
4.5.	Setup	40
4.5.1.	Live avalanche photodiode mode	41
4.6.	Measurements and discussion	41
5.	Summary and outlook	45
A.	Acronyms	49
	Bibliography	51

List of Figures

1.1.	Complete experimental setup	2
2.1.	Droplet etched GaAs quantum dots.	4
2.2.	Biexciton-esciton cascade in a QD. [6]	5
2.3.	Fine structure splitting in a GaAs quantum dot.	5
2.4.	Absorption line shape of an electronic excitation.	6
2.5.	Zero-phonon line and phonon sideband. [11]	7
2.6.	Optical pumping of a QD by (a) above-band excitation and (b) resonant excitation [6] .	10
2.7.	Resonant two photon excitation [5]	11
2.8.	Hanbury-Brown-Twiss HBT experiment [5]	12
3.1.	A chirped sinusoidal wave which increases in frequency over time.	14
3.2.	Schematics of an interferometric autocorrelator	16
3.3.	Scheme of a folded pulse expander as described by Martinez [21]	17
3.4.	Final biexciton occupation after chirped Gaussian pulse of pulse duration $\tau_0 = 2 \text{ ps}$.	18
3.5.	Electric field E of Gaussian laser pulse of pulse duration $\tau_0 = 0.5 \text{ ps}$ for chirp of (a) $\alpha = 0 \text{ ps}^2$ and (b) $\alpha = 0.5 \text{ ps}^2$	19
3.6.	Intensity of IAC of a Gaussian laser pulse of pulse duration $\tau_0 = 0.5 \text{ ps}$ with applied MOSAIC filter for chirp of (a) $\alpha = 0 \text{ ps}^2$ and (b) $\alpha = 0.5 \text{ ps}^2$	19
3.7.	Intensity of IAC of a Gaussian laser pulse of pulse duration $\tau_0 = 0.5 \text{ ps}$ with applied MOSAIC filter for chirp of (a) $\alpha = 0 \text{ ps}^2$ and (b) $\alpha = 0.5 \text{ ps}^2$	20
3.8.	Intensity of IAC of a Gaussian laser pulse of pulse duration $\tau_0 = 0.5 \text{ ps}$ with applied MOSAIC filter for chirp of (a) $\alpha = 0 \text{ ps}^2$ and (b) $\alpha = 0.5 \text{ ps}^2$. The orange dots are results of a numerical peak finder algorithm, executed in order to find local minima.	20
3.9.	Intensity of IAC of a Gaussian laser pulse of pulse duration $\tau_0 = 0.5 \text{ ps}$ with applied MOSAIC filter and fitted α -values.	21

3.10. Measured IAC of Ti:Sa Laser without (a) and with (b) pulse expander before the autocorrelator	22
3.11. Measured IAC of Ti:Sa Laser with applied MOSAIC filter without (a) and with (b) pulse expander before the autocorrelator	22
4.1. A Gaussian beam near its beam waist.	25
4.2. Gaussian modes higher order of a simple Ti-sapphire laser	27
4.3. Fabry P��rot interferometer with electric field mirror reflectivities r_1 and r_2	29
4.4. Airy distribution A'_{trans}	30
4.5. Demonstration of the physical meaning of the Airy finesse F_{Airy}	31
4.6. Incident monochromatic beam of light exciting transverse mode m, n of a resonator [28]	32
4.7. Mode matching of an Gaussian beam into a Fabry P��rot interferometer.	33
4.8. Spatial filtering of Gauss modes.	35
4.9. Simulated exciton emission of a GaAs quantum dot	37
4.10. Transmission of the FPI modes A'_{trans} compared to the exciton emission $\Phi_{dot}(E)$ for (a) ZPL and (b) PSB.	37
4.11. Transmissions of the FPI modes A'_{trans} for different mirror distances $l - m \cdot \Delta l$ with $m \in \mathbb{N}$ compared to the exciton emission $\Phi_{dot}(E)$	38
4.12. Output-photon-flux of the scanning FPI $\Phi_{fabry,perot}(E)$ compared to the exciton emission $\Phi_{dot}(E)$ for (a) ZPl and (b) PSB.	38
4.13. Output-photon-flux of the scanning FPI $\Phi_{fabry,perot}(E)$ compared to the exciton emission $\Phi_{dot}(E)$. In (a) $\Phi_{fabry,perot}(E)$ is $\Phi_{dot}(E)$, then in (b) the absolute difference $ \Phi_{fabry,perot,shifted}(\nu) - \Phi_{dot}(\nu) $ is displayed $ \Phi_{fabry,perot,shifted}(\nu) - \Phi_{dot}(\nu) $	39
4.14. Scanning Fabry P��rot interferometer	40
4.15. Live avalanche photodiode setup	41
4.16. Aligning the Fabry P��rot interferometer	42
4.17. Transmission measurement of FPI with ground mirror distance $l \approx 2$ mm and HeNe laser. (a) was aligned without spatial filtering with a pinhole and (b) involved a pinhole.	42
4.18. Polarization map of exciton of QD in sample AS208.	43
4.19. Finestructure measurement of biexcition of QD in sample AS208 by passing thorugh FPI and sweeping the mirror distance. Ground mirror distance was $l \approx 2$ mm.	43

1. Introduction

In the past century, technology was transformed by the first quantum revolution. Scientists and engineers all around the world utilized certain features of quantum mechanics such as energy quantization and wave-particle duality to create devices which are a nowadays a fixed part of everyone's life. These technologies, ranging from semiconductor devices to LEDs and lasers, became high-performance components which drive the global communication networks. In contrast to the first quantum revolution, the second quantum revolution will make use of superposition, entanglement and quantum measurement [1]. It will provide quantum simulations as well as secure communication via quantum key distribution (QKD). QKD enables to produce a shared random key, which only the two parties wishing to exchange messages know, and which can be used by one of them to encrypt a message and be used by the other to decrypt it. It even allows to detect eavesdropping when quantum entanglement is implemented. However, this requires deterministic sources of single entangled photons.

With this motivation in mind, droplet-etched GaAs quantum dots as potential sources are investigated, as they are quasi strain-free, of high symmetry and exhibit low values of fine structure splitting (FSS). Quantum dots can serve as emitters of single indistinguishable photons, yet entanglement fidelity is limited by the FSS between the two exciton states [2] and re-excitation of photons at the exciton level to the biexciton level before they can decay to the ground state. The FSS can be eliminated by using external perturbations [3] and re-excitation of the photons at the exciton level can be avoided by resonant two-photon excitation. With these measures on-demand generation of entangled photons gets within reach [4]. However, resonant two-photon excitation requires precise control of the intensity of the exciting field in order to inverse the quantum dot from the ground state to the biexciton state. Exciting via adiabatic rapid passage with frequency-chirped pulses can be an alternative, which is further discussed in chapter 3. When it comes to characterizing quantum dot (QD) emission, more obstacles arise as fine features of the emission spectrum are not resolvable with a CCD-based spectrometer only. However, a small-band bandpass filter with adjustable center frequency could

1. Introduction

scan through the ranges of interest and its output could then be recorded with the CCD. Chapter 4 describes the efforts to build up a scanning Fabry-Pérot interferometer to do exactly that.

1.1. Setup

The setup used for the measurements described in following chapters is sketched in figure 1.1. The reader might want to return to this section when parts of the setup are discussed.

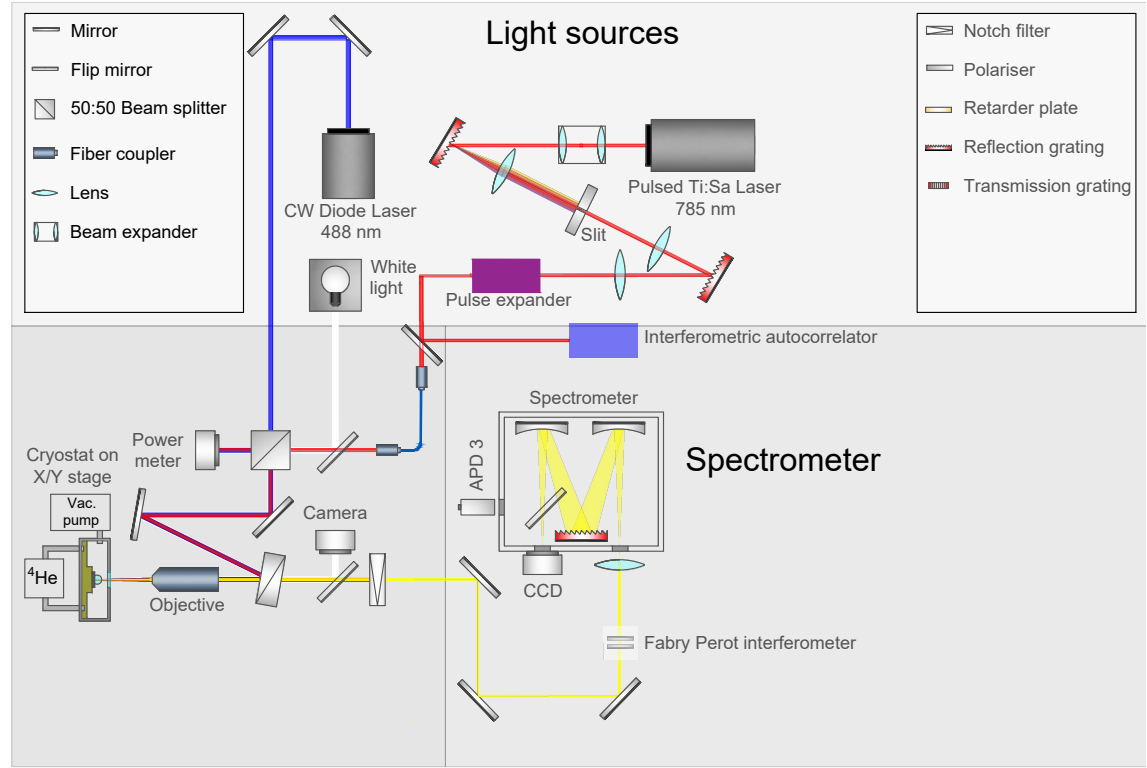


Figure 1.1.: Complete experimental setup, which was used in order to quantify the chirp of the Ti:Sa Laser and resolve spectral emission of a quantum dot [5].

2. Droplet etched gallium arsenide quantum dots

2.1. Fabrication and optical properties

Quantum dots (QD) are nanostructures which confine the motion of electrons and holes in all three spatial dimensions. Confinement results in discrete energy levels, which is why QDs are sometimes referred to as *artificial atoms*. The discussion in this section is based on the PhD thesis of Huber [6].

Gallium arsenide QDs investigated within this master's thesis are grown by molecular beam epitaxy (MBE) with the self-assembled nanodrill technology described in the work of Wang et al. [7]. As displayed in figure 2.1a the Al forms droplets on AlGaAs after evaporation. The Al reacts with AlGaAs, which leads into nanoholes etched into the surface. Under optimal conditions, these nanoholes are highly symmetric as can be seen in figure 2.1b. This results into QDs with high in-plane symmetry. The next step is the annealing process in which GaAs is deposited to fill the nanoholes. The QD is finalized by capping the layer with AlGaAs acting as top barrier.

Compared to the band gap of the host material $\text{Al}_{0.4}\text{Ga}_{0.6}\text{As}$ of 1.92 eV at room temperature, the core of the QD, GaAs has a band gap of only 1.42 eV at room temperature. This energy difference between the band gaps and the nanosized dimensions of the QD are responsible for the 3D confinement and the type-I band alignment depicted in figure 2.1c. Inside of the QD, optical transitions are possible. Transitions between the first energy level in the conduction band (CB) and the valence band (VB), often called the s-shell, are here of especially great interest. The carriers involved are the electrons e^- and the holes left behind h^+ . These are fermions and therefore only up to two of them can, in accordance with Pauli's exclusion principle, occupy a single energy state. Electrons and holes are strongly localized inside the QD and interact with each other by Coulomb interaction. This leads to

2. Droplet etched gallium arsenide quantum dots

multi-particle complexes with the most fundamental being the exciton (X), a bound state of an electron and a hole. A fully occupied s-shell, can be described by the quasiparticle called biexciton (XX).

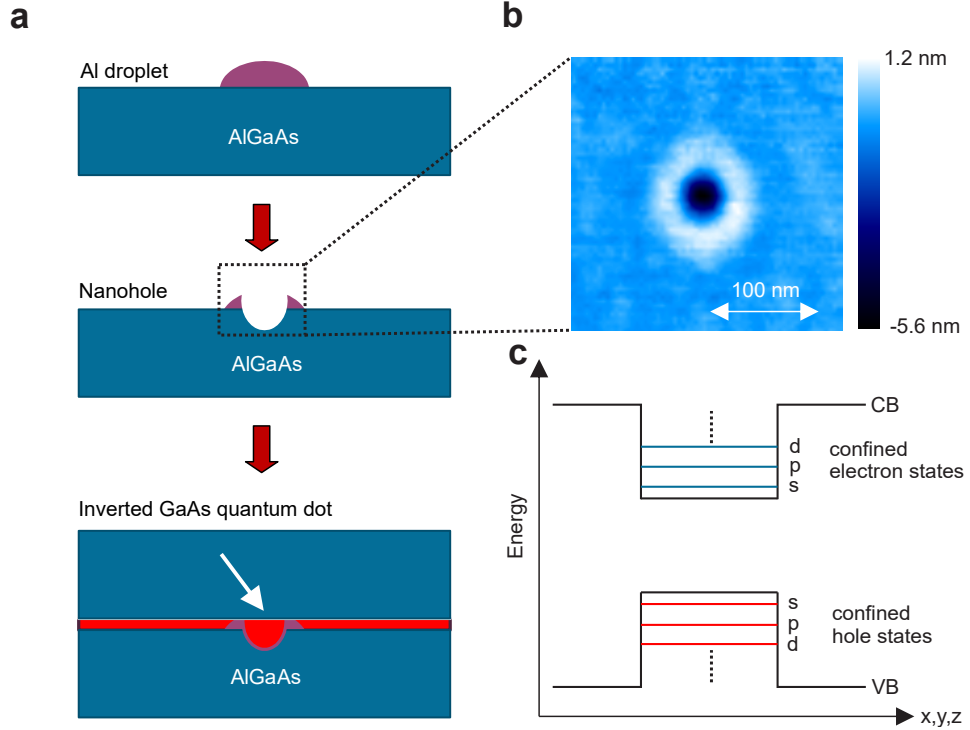


Figure 2.1.: (a) The growth process of a GaAs quantum dot by MBE.
 (b) Atomic force microscopy (AFM) image of the nanohole before it is filled with GaAs.
 (c) Conduction band (CB) and valence band (VB) of an optically active QD. [6]

In a QD, polarization-entangled photon pairs can be generated via a biexciton-exciton cascade [8], illustrated in figure 2.2. $|XX\rangle$ forms a full shell, which means that the total angular momentum projection along the quantization axis of the XX complex sums up to $M = 0$. After exciting the QD into the $|XX\rangle$ state (e.g. by optical pumping) it decays by spontaneous recombination of an electron-hole-pair accompanied by the emission of a single photon into the $|X\rangle$ state. The two dipole-allowed radiative transitions lead to only two possible $|X\rangle$ states:

- $| -1 \rangle$ under emission of a right-circularly-polarized photon $|R_{XX}\rangle$
- $| +1 \rangle$ under emission of a left-circularly-polarized photon $|L_{XX}\rangle$

$| -1 \rangle$ and $| +1 \rangle$ are degenerated in energy and decay into the groundstate $|G\rangle$ under emission of $|L_X\rangle$

2.1. Fabrication and optical properties

and $|R_X\rangle$, respectively. The resulting state is then described by

$$|\psi^+\rangle = \frac{1}{\sqrt{2}} (|L_{XX}\rangle |R_X\rangle + |R_{XX}|L_X\rangle) \quad (2.1)$$

which is one of the Bell states, representing the maximal entangled states.

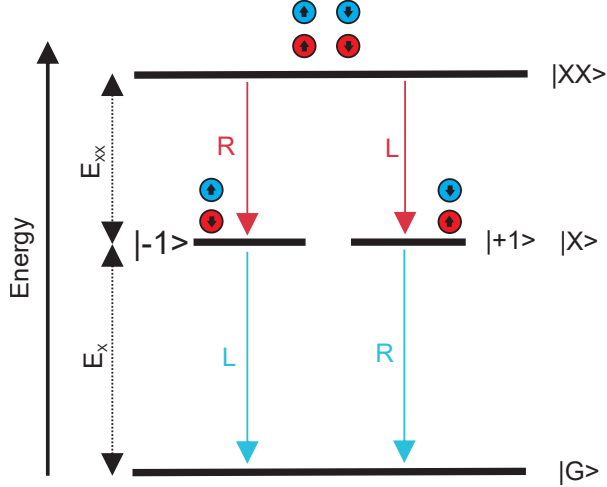
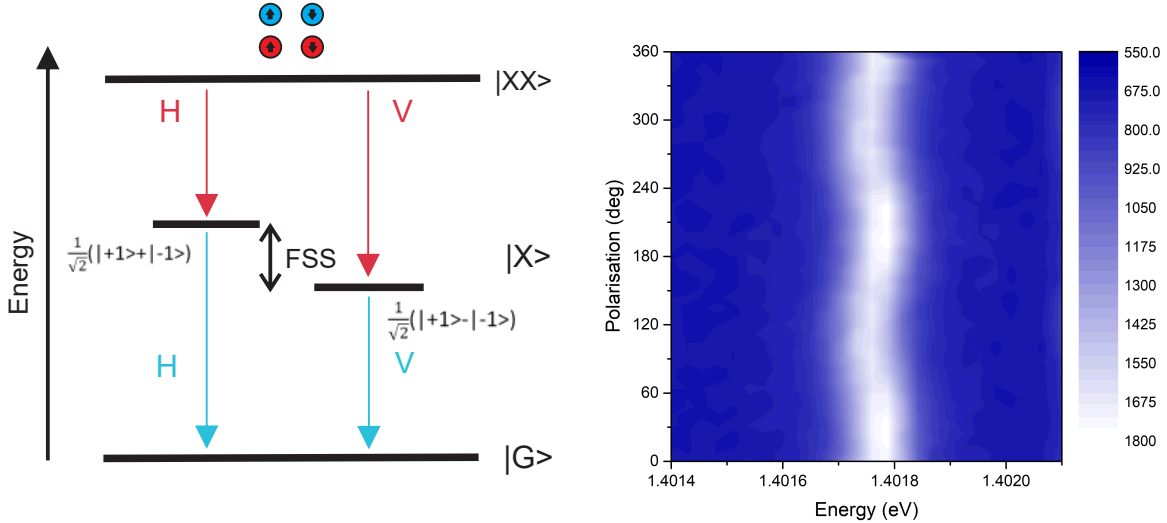


Figure 2.2.: Biexciton-esciton cascade in a QD. [6]



(a) XX decay cascade without X degeneracy because of fine structure splitting. [6]

(b) Photoluminescence spectra of X emission of a GaAs Qd plotted for different polarizer angles. In the image the effect of the linear polarization of the fine structure components is visible. [5]

Figure 2.3.: Fine structure splitting in a GaAs quantum dot.

2.2. Fine structure splitting

Fine structure splitting (FSS) in a QD describes the energy splitting between the two possible bright $|X\rangle$ states. In GaAs it originates from the exchange interaction between electrons and holes. [2].

In figure 2.3a the $|XX\rangle$ decay path with splitted $|X\rangle$ eigenstates is shown. $|XX\rangle$ exhibit no splitting as the angular momentum of the electrons and holes add to zero and therefore no exchange interaction occurs. In figure 2.3b photoluminescence spectra recorded with a linear polarizer are shown.

2.3. Zero-phonon line and phonon sideband

The excitonic emission of GaAs QDs exhibits non-Lorentzian asymmetric broadening. As shown by Peter et al. [9] these side bands can be traced back to a coupling to acoustic phonons. The discussion of phonon side bands (PSBs) is based on the works of Friedrich and Haarer [10] and Peter et al. [9].

Figure 2.4 displays a schematic representation of the zero phonon line (ZPL) and PSB absorption spectrum. The intensity distribution between the two components depends strongly on temperature.

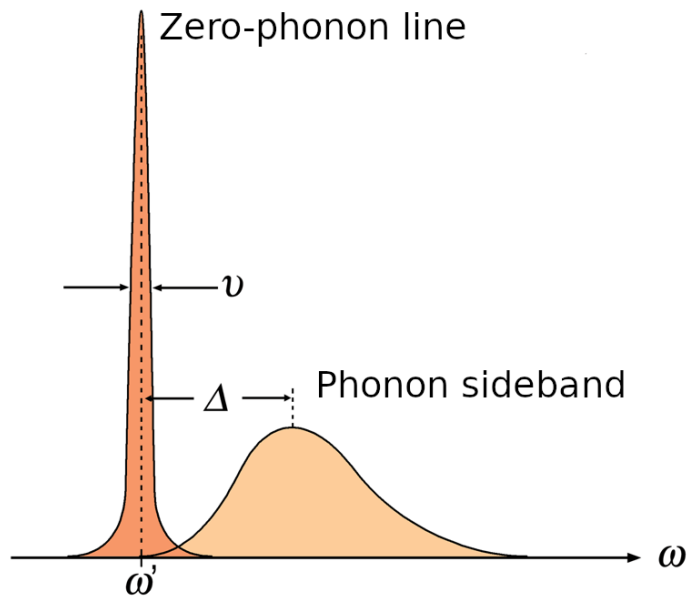
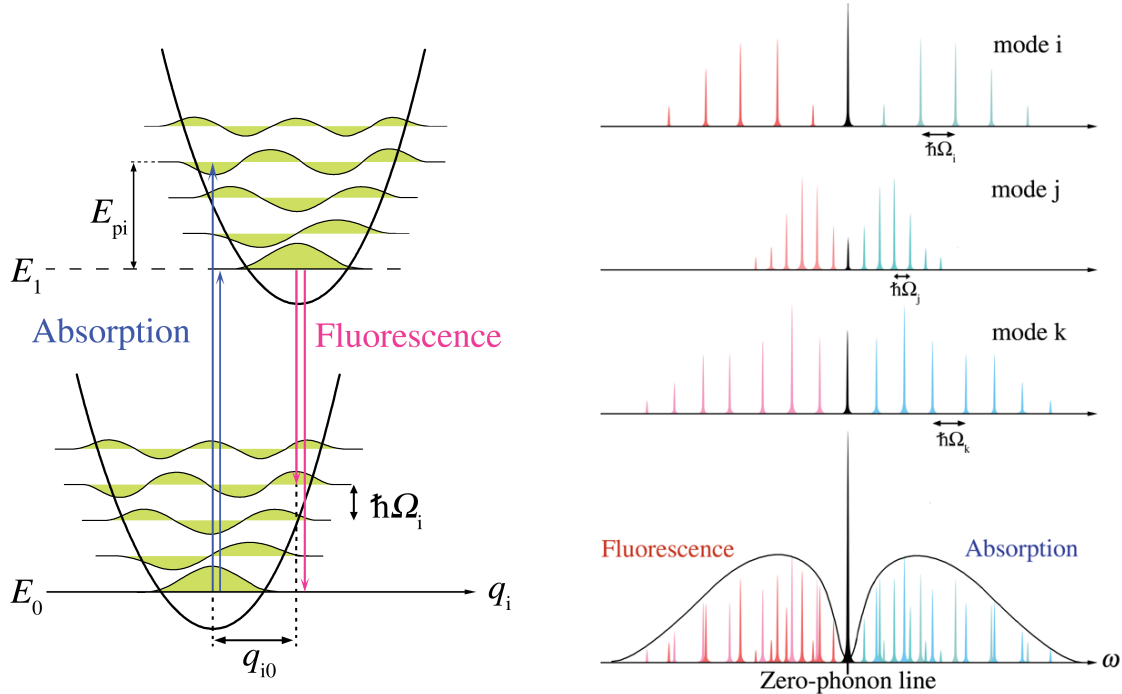


Figure 2.4.: Absorption line shape of an electronic excitation. The emission is mirrored at ω' .

To determine the frequency gap Δ in figure 2.4, the Franc-Condon principles are used. They state that electronic transition between ground and excited state is much faster than the motion in the lattice. Hence, there is no motion along the configurational coordinates q_i during the energy transitions as depicted in figure 2.5a. The transitions can be displayed as vertical arrows with the shorter arrow describing the ZPL and the longer one describing the PSB. According to the Franc-Condon principles, the more the wave functions of two vibrational energy levels overlap, the likelier is the electronic transition between these two. In the case of figure 2.5a this occurs when the photon energy equals to the energy difference $E_1 - E_0$ plus three quanta of vibrational energy $E_{pi} = \hbar\Omega_i$. The emission follows the same principle.



(a) Energy spectrum of a two-level electronic system with phonon coupling. The arrows describe emission/absorption with and without phonons respectively.

(b) Three lattice normal modes (i, j, k) and the resulting emission/absorption spectrum.

Figure 2.5.: Zero-phonon line and phonon sideband. [11]

Figure 2.5a and 2.5b implicitly assume approximations in addition to the Franck-Condon principles. The lattice vibrational mode has to be well described by a quantum harmonic oscillator. Additionally, it is assumed that only the lowest lattice vibration is excited and that the harmonic oscillator potentials are equal in both states. These preconditions are visible in the parabolic shaped potential wells and

2. Droplet etched gallium arsenide quantum dots

equally spaced phonon energy levels in figure 2.5a.

The reason why zero-phonon line is stronger than the phonon side band can be found by examining the superposition of the lattice modes. Each lattice mode m leads to a different energy difference $\hbar\Omega_m$ between phonons. That is why the transitions with phonons result in a energy distribution and the zero-phonon transition add up at the electronic origin $E_1 - E_0$ as can be seen in figure 2.5bb.

The theoretical limit of the spectral range of the zero-phonon line for a GaAs quantum dot can be calculated with the time-energy uncertainty relation

$$\Delta E \cdot \Delta t = \frac{h}{2\pi} \quad (2.2)$$

This gives for typical lifetime of a GaAs quantum dot of $\Delta t = 250$ ps

$$\Delta E = 2.64 \text{ } \mu\text{eV}. \quad (2.3)$$

The frequency uncertainty can be obtained through

$$\Delta\nu = \frac{\Delta E}{h}. \quad (2.4)$$

The wavelength λ relates to ν with the Planck-Einstein relation

$$\lambda(\nu) = \frac{c}{\nu} \quad (2.5)$$

and the wavelength uncertainty $\Delta\lambda$ can be approximated with a Taylor series around ν_0

$$\Delta\lambda = -\lambda'(\nu_0) \cdot \Delta\nu. \quad (2.6)$$

With equation (2.4) and the center wavelength of the zero-phonon line λ_0 in table 2.1 this gives

$$\Delta\lambda = \frac{c}{\nu_0^2} \cdot \Delta\nu = \frac{\lambda_0^2}{c} \cdot \Delta\nu \quad (2.7)$$

$$\approx 1.0 \text{ pm} \quad (2.8)$$

Together with data from Schöll et al. [12] and empirical values measured by this group, this leads to the parameters listed in table 2.1.

Table 2.1.: Parameters of GaAs quantum dots used in the laboratory of semiconductor physics department in Linz. Zero-phonon line calculates from the theoretical limit according to the life time of the excitonic state (as can be seen in equation (2.8)) up to broader lines which are still valued enough to be measured. The phonon sideband resembles data taken from Schöll et al. [12].

Quantum dot emission	Center wavelength λ_0	Spectral range $\Delta\lambda$	Waveform
Zero-phonon line	(700 to 800) nm	(1.0 to 1.4) pm	Cauchy
Phonon sideband	~0.25 nm higher than zero-phonon line	500 pm	Gauss

2.4. Optical excitation of a quantum dot

In this section, the different ways of optically exciting QDs are discussed. It is based on the PhD thesis of Huber [6] and the master's thesis of Schimpf [5]. The excited state of a QD can be populated in various ways. A common way is the above-band excitation, depicted in figure 2.6a. Electrons are optically excited by a laser with energies above the band gap of the QDs host material $\text{Al}_{0.4}\text{Ga}_{0.6}\text{As}$ with $E_L = 1.92 \text{ eV}$ at room temperature. Subsequently, the electrons are captured by the QDs and relax via phonon-scattering to the lowest energy level, the s-shell. However, because of pronounced recapture processes [13] and spin scattering processes [14], above-band excitation is not favourable for entangled photon generation. Additionally, indistinguishability of the emitted photons is reduced because of carrier-relaxation-induced time-jitter and fluctuating electric fields. As this team is interested in extracting entangled X/XX photon pairs, above-band is often not the best exciting technique for GaAs QDs. Resonant excitation of electron-hole pairs provides an alternative which does not suffer from the mentioned problems with above-band excitation. As shown in figure 2.6b this technique creates electron-hole-pairs directly in the s-shell.

2. Droplet etched gallium arsenide quantum dots

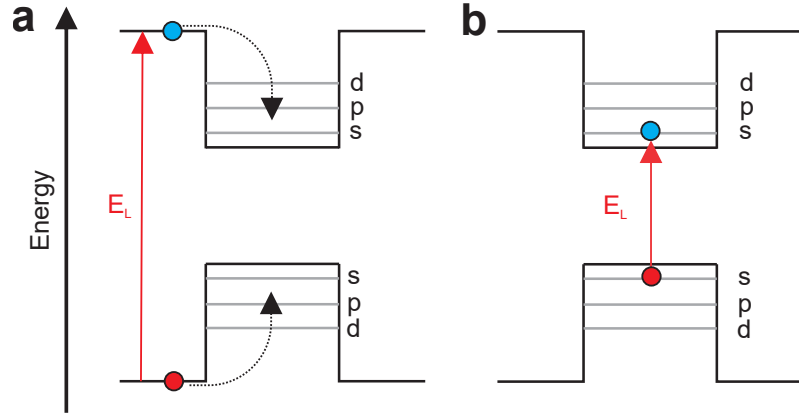


Figure 2.6.: Optical pumping of a QD by (a) above-band excitation and (b) resonant excitation [6]

Due to dipole-selection rules, resonant population of the $|XX\rangle$ state requires a two-photon-absorption process. Hereby, the energy of a femtosecond-pulse laser E_p is tuned to exactly the half of the XX energy with respect to the ground energy, as sketched in figure 2.7a. Because of Coulomb interaction, two times the X energy with respect to the ground energy $2 \cdot E_X$ is not equal to E_{XX} but differs by the binding energy E_B . The laser is therefore tuned to

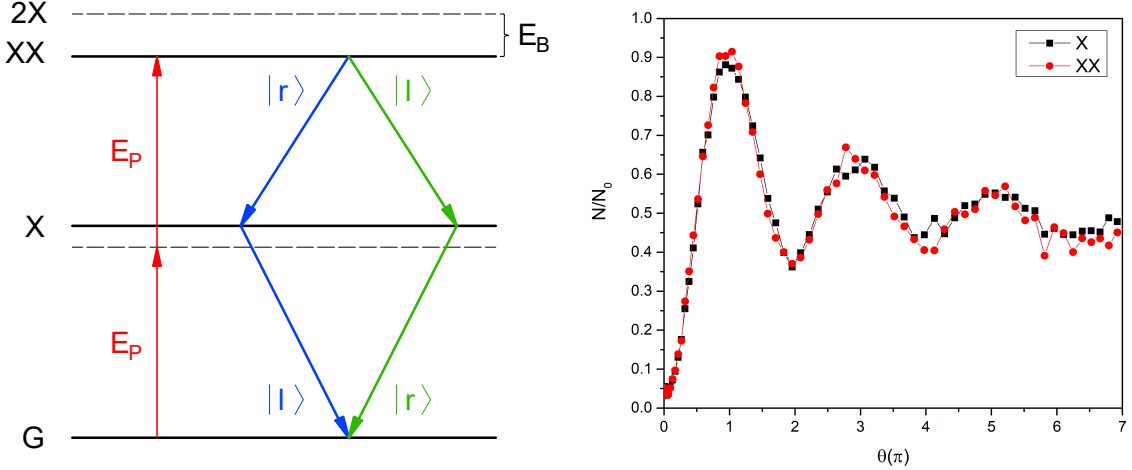
$$E_p = E_X - E_B/2. \quad (2.9)$$

Empirically $E_B \approx 3.78$ meV for GaAs QDs. Resonant two-photon absorption is a third-order non-linear effect which involves two photons and electrons at once. It depends on the third-order-susceptibility $\chi^{(3)}$ of GaAs and therefore requires relatively high laser power.

As this two-level system is driven in resonance its population exhibits Rabi oscillations. The final population of the XX can be described by

$$N_{XX} = \sin^2\left(\frac{\theta}{2}\right) \quad (2.10)$$

with θ as the pulse area in relation to the Rabi oscillations. θ is not the area of the excitation pulse, but depends on it in a non-trivial way [15]. Measured Rabi oscillations of X and XX are shown in figure 2.7b [16]. Theoretically, the curve should oscillate between occupancies N/N_0 of 0 and 1. However, as a consequence of phonon damping the occupancy converges to a purely probabilistic value of 0.5 [17].



(a) Resonant two photon excitation of XX.

 The laser is tuned to $E_P = E_{XX}/2$.

 (b) Rabi oscillations of X and XX as a function of the pulse area θ .

 N/N_0 is the occupancy and N_0 the maximum population.

Figure 2.7.: Resonant two photon excitation [5]

2.5. Single photon emission

The XX-X cascade shown in figure 2.7a results in a single photon pair per emission cycle. Single photons are necessary for quantum cryptography and quantum optics in general which motivates the following discussion of this topic based on the thesis of Huber [6]. The single photon purity of the $|XX\rangle$ to $|X\rangle$ and the $|X\rangle$ to $|G\rangle$ signals, respectively, can be determined by performing a Hanbury-Brown-Twiss (HBT) experiment. A HBT setup is shown in figure 2.8a and it allows to measure the second-order correlation function, which is defined as

$$g^{(2)} = \frac{\langle I(t)I(t+\tau) \rangle}{\langle I(t) \rangle \langle I(t+\tau) \rangle} \quad (2.11)$$

with $I(t)$ as the light intensity and τ as the time delay. When a single photon enters the input of the beam splitter (BS) it can only be measured at one output, but never at both simultaneously. Assuming a perfect single photon emitter, a coincidence measurement between APD1 and APD2 will result in $g^{(2)}(\tau) = 0$ at zero time delay. Subsequently, side peaks are expected which are correlated to the repetition rate R of the laser by $\tau_s = z/R$ with $z \in \mathbb{Z} \setminus \{0\}$. The single photon purity can then be defined as

$$\kappa(b) = \frac{A_0(b)}{A_s(b)} \quad (2.12)$$

2. Droplet etched gallium arsenide quantum dots

with A_0 as the area under $g^{(2)}(\tau)$ around $\tau = 0$ and A_s as the average area under the side peaks at τ_s . The time bin b has to be chosen so that it includes a full side peak. If b would be chosen too small it would falsely increase κ , if chosen too high it includes unnecessary much noise.

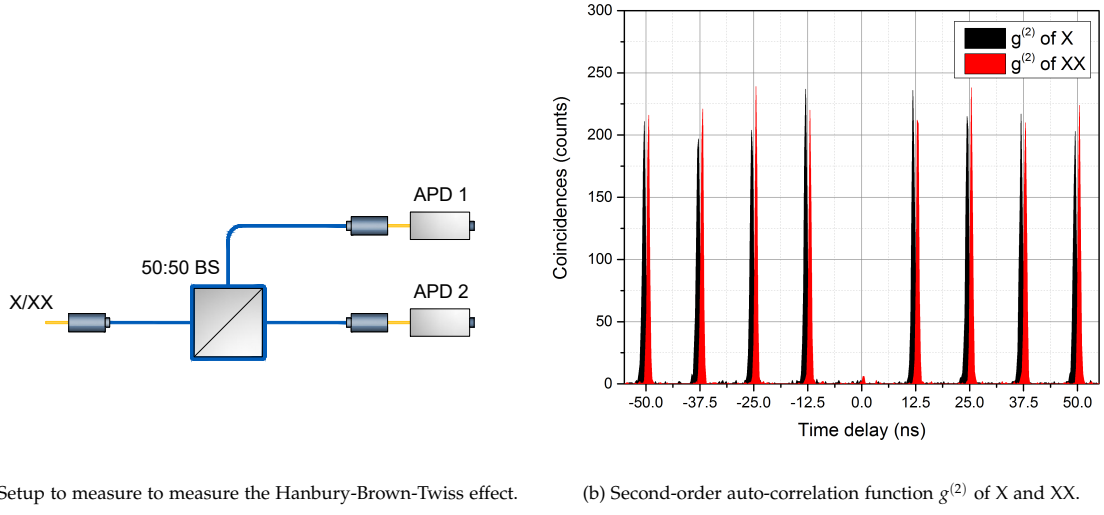


Figure 2.8.: Hanbury-Brown-Twiss HBT experiment [5]

3. Entangled photon generation using adiabatic rapid passage with frequency-chirped pulses

3.1. Introduction and motivation

In order to efficiently use the biexciton decay cascade, the biexciton state has to be prepared beforehand in a robust way. This chapter deals with the efficient inversion of the QD from the ground state to the biexciton level via adiabatic rapid passage (ARP). ARP uses chirped pulses, which need to be measured and deterministically adjusted in order to effectively use them. Therefore, the majority of this chapter will focus on the chirp and how to determine and adjust it, with the help of simulations and later with measurements.

3.2. Chirp

A chirped signal is a signal of which the frequency changes over time. For example, the frequency of a linearly chirped signal $f(t)$ would be described by

$$f(t) = ct + f_0 \quad (3.1)$$

where f_0 is the starting frequency at $t = 0$ and c is the chirpiness. A linear chirped sinusoidal wave is depicted in figure 3.1.

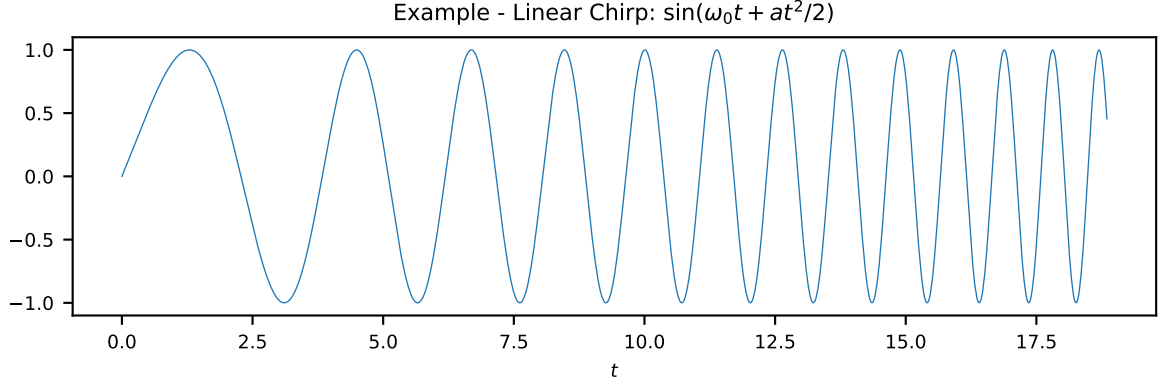


Figure 3.1.: A chirped sinusoidal wave which increases in frequency over time.

As this chapter is concentrated on exciting QDs with frequency-chirped pulses, the mathematical description of chirped laser pulses will now be discussed. The electric field of a laser $E(t)$ has the shape

$$E(t) \sim \text{Re} \left(f^{1/2}(t) \cdot \exp(-i\omega t - i\phi(t)) \right) \quad (3.2)$$

with the central frequency ω and the linear chirp $\phi(t)$.

Depending on the laser either a Gaussian or a hyperbolic secant describes the pulse shape more accurately [18, 19]

- Gaussian pulse:

- Pulse shape of

$$f_{gauss}(t) = \left(\frac{A_{gauss}}{\sqrt{2 \cdot \pi \cdot \tau_0 \cdot \tau}} \exp\left(-\frac{t^2}{2 \cdot \tau^2}\right) \right)^2 \quad (3.3)$$

with the normalization constant A_{gauss} , the pulse duration τ_0 , the central frequency ω and the chirp coefficient α .

- Linear chirp of

$$\phi_{gauss}(t) = \frac{a_{gauss} t^2}{2} \quad (3.4)$$

where $\tau = \sqrt{\alpha^2 / \tau_0^2 + \tau_0^2}$ characterizes the chirped pulse length and $a = \alpha / (\alpha^2 + \tau_0^4)$ is the frequency chirp rate.

- Secant pulse:

- Pulse shape of

$$f_{secant}(t) = A_{secant} \cdot \operatorname{sech}^2\left(\frac{t}{\tau_0}\right) = A_{secant} \cdot \left(\frac{2}{\exp(\frac{t}{\tau_0}) + \exp(-\frac{t}{\tau_0})}\right)^2 \quad (3.5)$$

with the normalization constant A_{secant} , the pulse duration τ_0 , the central frequency ω and the chirp coefficient α .

- Linear chirp of

$$\phi_{secant}(t) = \alpha_{secant} \left(\frac{t}{\tau_0}\right)^2 \quad (3.6)$$

The following discussion in this chapter will assume laser pulses with a Gaussian shape.

3.3. Measuring the chirp with interferometric autocorrelation

In order to estimate the pulse width τ_0 interferometric autocorrelation (IAC) is used. Basically, a nonlinear crystal is added to a Michelson interferometer in order to generate a signal governed by

$$I_M(\tau) = \int_{-\infty}^{+\infty} \langle |(E(t) + E(t - \tau))^2|^2 \rangle dt. \quad (3.7)$$

Here $\langle \rangle$ denotes averaging over fast oscillations of the electric field and the integral stands for integration over the pulse envelope. Under the use of equation 3.2 it can be expanded to

$$I_M(\tau) = 1 + 2 \int f(t)f(t + \tau)dt + \int f(t)f(t + \tau)\cos(2\omega\tau + 2\Delta\phi)dt \\ + 2 \int f^{1/2}(t)f^{3/2}(t + \tau)\cos(\omega\tau + \Delta\phi)dt + 2 \int f^{3/2}(t)f^{2/2}(t + \tau)\cos(\omega\tau + \Delta\phi)dt \quad (3.8)$$

where $\Delta\phi(t, \tau) = \phi(t + \tau) - \phi(t)$ and $\int f(t)dt = 1$.

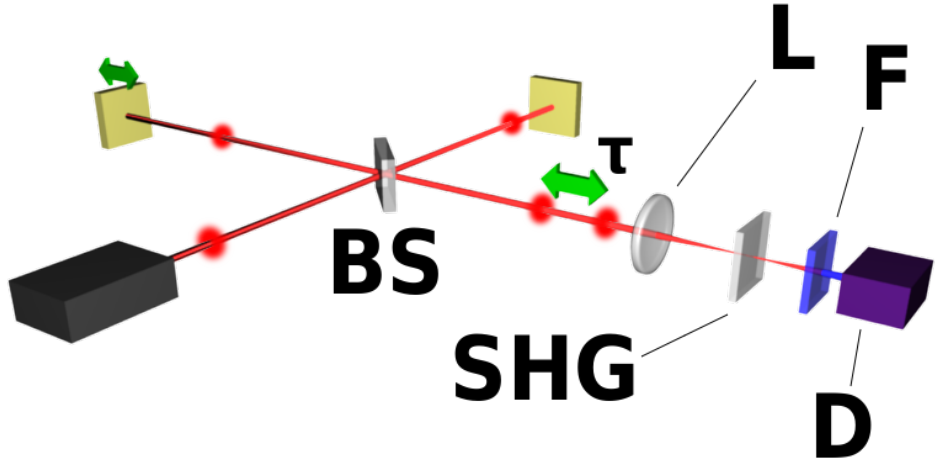


Figure 3.2.: Schematics of an interferometric autocorrelator, where **L** is a converging lens, **SHG** a second-harmonic generation crystal, **BS** a beam splitter and **F** a spectral filter to block the fundamental wavelength [20].

As will be shown in section 3.6 the chirp parameter α has hardly any measurable influence on the resulting signal. However, certain modifications to the IAC signal introduced by Hirayama and Sheik-Bahae [19] make it much more sensitive to the temporal chirp. It is called modified-spectrum autointerferometric correlation (MOSAIC) and it performs the following transformations on the IAC spectrum: the ω terms are eliminated and the 2ω term is doubled. The MOSAIC signal is then described by the following equation

$$I_{M,filtered}(\tau) = 1 + 2 \int f(t)f(t + \tau)dt + 2 \int f(t)f(t + \tau)\cos(2\omega\tau + 2\Delta\phi)dt \quad (3.9)$$

3.4. Deterministically adjusting the chirp with a pulse expander

In the optimal case the chirp of the pulse can be deterministically adjusted in order to most efficiently excite the QD via adiabatic rapid passage (which will be introduced in section 3.5). Grating compressors as discussed by Martinez [21] were originally used to compensate the broadening of fibers. However, together with a telescope they have the inverse effect and can be used to induce a positive chirp. A setup like this is sketched in figure 3.3 and it will in future references in this work be called *pulse expander*. The accumulated group velocity dispersion introduced by the pulse expander is described by

$$\frac{d^2\Phi}{d\omega^2} = k\beta^2 2z \quad (3.10)$$

where z is the (adjustable) distance between the grating and focal plane of the lens and β depends on the parameters of the grating and the lens.

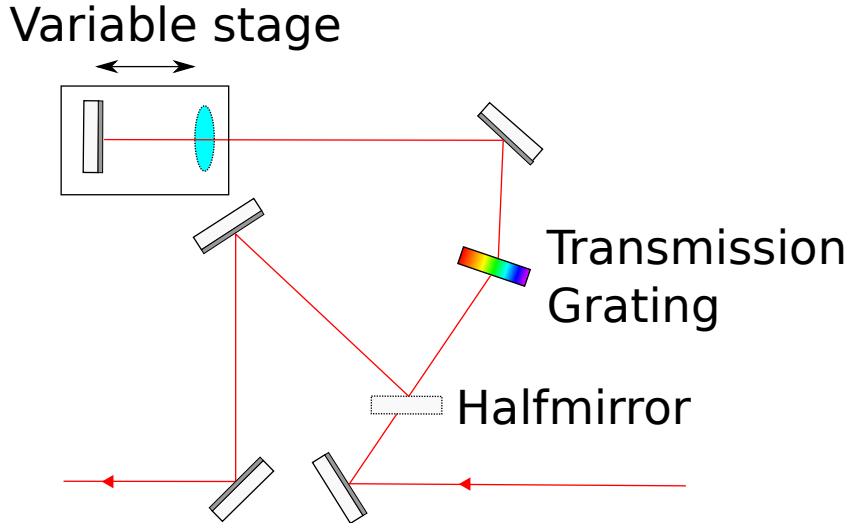


Figure 3.3.: Scheme of a folded pulse expander as described by Martinez [21]

3.5. Adiabatic rapid passage

One way to inverse the QD from the ground state to the biexciton state is by exciting it with a transform-limited laser pulse of constant centre frequency, which is equals to half of the ground state biexciton transition frequency. However, in order to ensure the inversion, precise control of the field intensity is required [18]. Adiabatic rapid passage (ARP) with frequency chirped is an alternative to this Rabi-flopping scheme. Basically, the goal is to adiabatically excite from ground state to biexciton state without energy-level crossing [22]. Schemes which provide that, are also stable with respect to intensity changes of the laser field.

In order to calculate the final biexciton occupation, Glässl et al. [18] assumed a linearly-chirped Gaussian laser pulse as discussed in section 3.2. The simulation results are visible in figure 3.4.

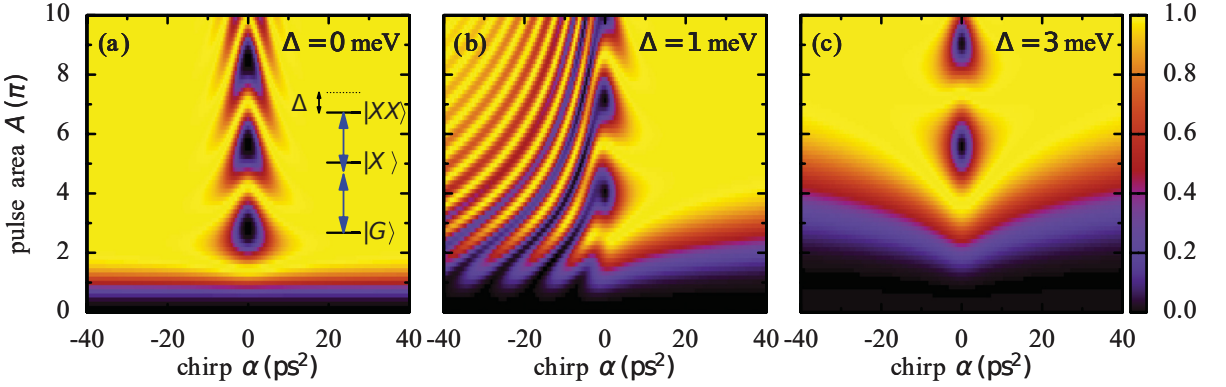


Figure 3.4.: Final biexciton occupation after chirped Gaussian pulse of pulse duration $\tau_0 = 2\text{ ps}$. It is plotted vertically as a function of the original pulse area A and vertically as a function of the chirp α for biexciton binding energies of (a) $\Delta = 0$, (b) 1 , and (c) 3 meV [18].

The central frequency is chosen so that for $\alpha = 0$ it resonates to ground state biexciton transition, which is sketched in figure 3.4. For $\alpha = 0$ Rabi oscillations are visible and its period depends strongly on the biexciton binding energy Δ . However, for $\alpha \gg 0$ biexciton preparation becomes insensitive to small variations to the pulse area A as long it exceeds a certain threshold. This is therefore the regime which would be the most suitable to work in. In the case of $\alpha < 0$ this insensitivity does not appear for moderate values of Δ as can be seen in figure 3.4(b).

3.6. Simulation

The electric field E of a chirped laser pulse is described by equation (3.2). The following discussion will assume a Gaussian laser shape as described by equation (3.3) and (3.4). A simulation for E is plotted for different chirp parameters α in figure 3.5. As can be seen there, the chirp parameter strongly influences the shape of the electric field. If E could be measured directly, the chirp could be easily estimated, but this is unfortunately not the case.

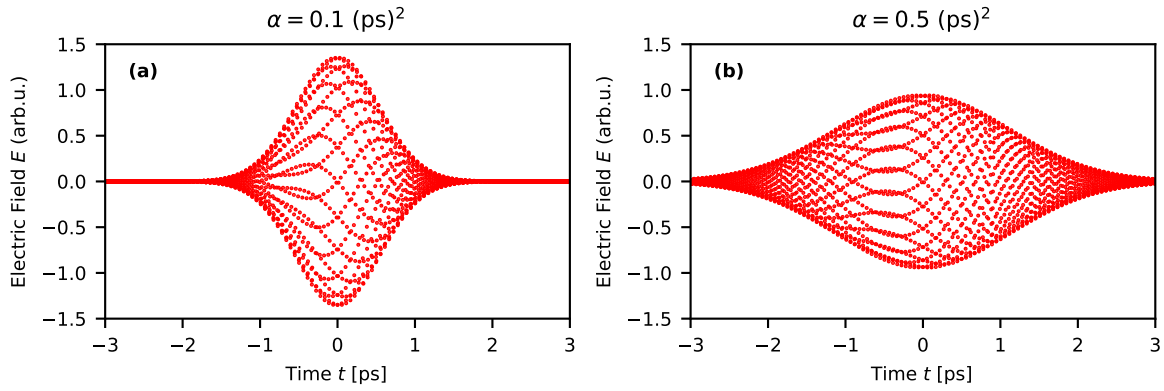


Figure 3.5.: Electric field E of Gaussian laser pulse of pulse duration $\tau_0 = 0.5$ ps for chirp of (a) $\alpha = 0 \text{ ps}^2$ and (b) $\alpha = 0.5 \text{ ps}^2$

What is possible is sending the laser into an IAC which outputs a signal as shown in figure 3.6 and described by equation (3.7). However, the chirp only marginally influences the resulting signal.

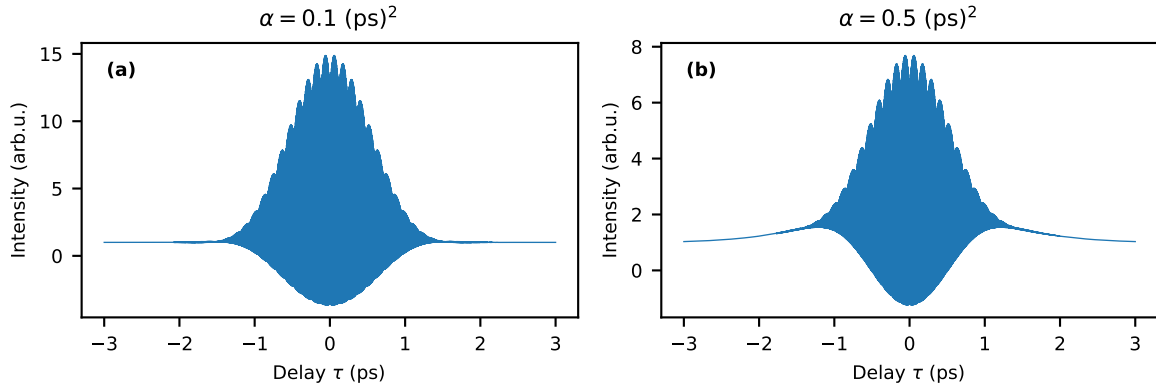


Figure 3.6.: Intensity of IAC of a Gaussian laser pulse of pulse duration $\tau_0 = 0.5$ ps with applied MOSAIC filter for chirp of (a) $\alpha = 0 \text{ ps}^2$ and (b) $\alpha = 0.5 \text{ ps}^2$

That is why the MOSAIC filter is applied which results in a signal as shown in figure 3.7 and described by equation (3.9). Now the influence of the chirp is clearly visible in the lower envelope.

3. Entangled photon generation using adiabatic rapid passage with frequency-chirped pulses

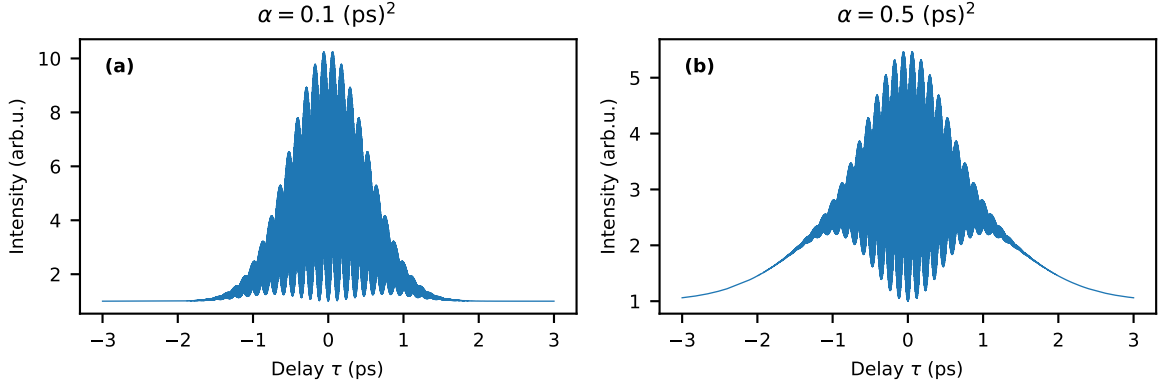


Figure 3.7.: Intensity of IAC of a Gaussian laser pulse of pulse duration $\tau_0 = 0.5 \text{ ps}$ with applied MOSAIC filter for chirp of (a) $\alpha = 0 \text{ ps}^2$ and (b) $\alpha = 0.5 \text{ ps}^2$

The points of the lower envelope can be obtained by determining the local minima of the signal as shown in figure 3.8.

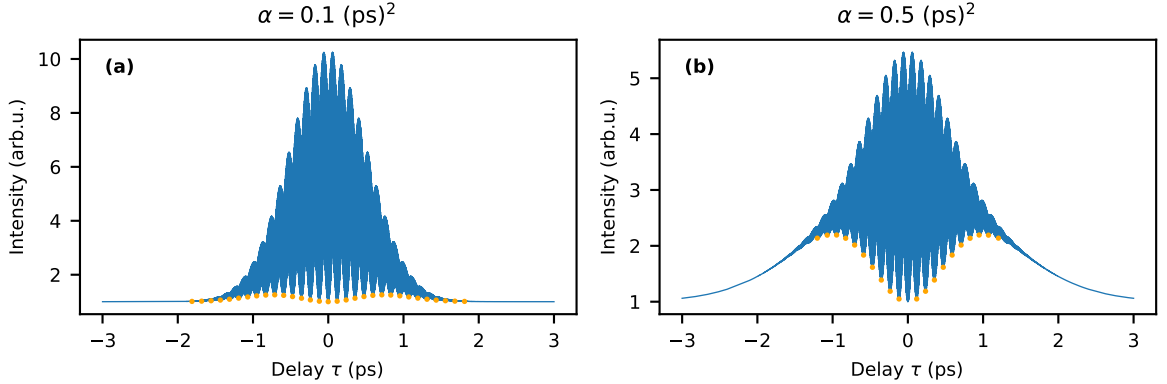


Figure 3.8.: Intensity of IAC of a Gaussian laser pulse of pulse duration $\tau_0 = 0.5 \text{ ps}$ with applied MOSAIC filter for chirp of (a) $\alpha = 0 \text{ ps}^2$ and (b) $\alpha = 0.5 \text{ ps}^2$. The orange dots are results of a numerical peak finder algorithm, executed in order to find local minima.

The lower bound (minima envelope) of the MOSAIC trace can be derived by use of the standard textbook procedure [23]

$$S_{\text{MOSAIC}}^{\min}(\tau) = 1 + 2 \cdot g(\tau) - 2 \cdot [g_s^2(\tau) + g_c^2(\tau)]^{1/2} \quad (3.11)$$

with

$$g(\tau) = \int f(t)f(t + \tau)dt \quad (3.12)$$

$$g_s(\tau) = \int f(t)f(t + \tau)\sin(2\Delta\phi)dt \quad (3.13)$$

$$g_c(\tau) = \int f(t)f(t + \tau)\cos(2\Delta\phi)dt \quad (3.14)$$

The points of the lower envelope determined before can now be fitted in order to obtain the chirp parameter α as shown in figure 3.9. It is visible that the fitted values of α correspond to the expected values.

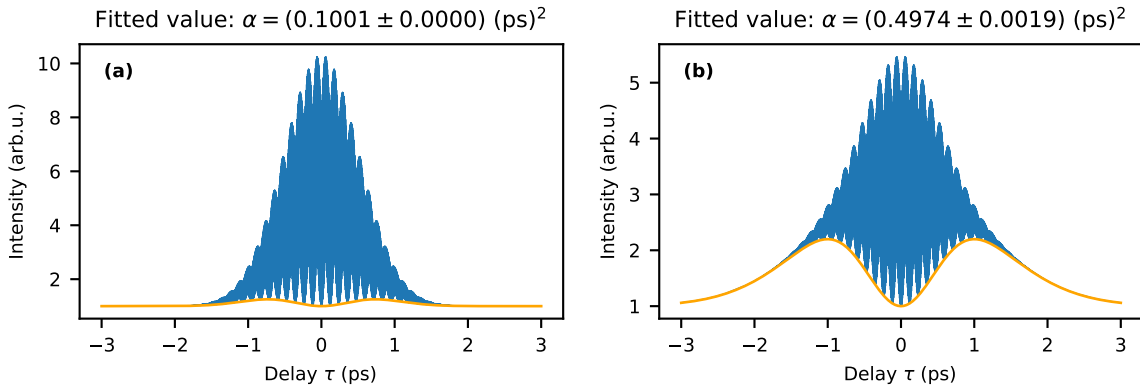


Figure 3.9.: Intensity of IAC of a Gaussian laser pulse of pulse duration $\tau_0 = 0.5 \text{ ps}$ with applied MOSAIC filter for chirp of (a) $\alpha = 0 \text{ ps}^2$ and (b) $\alpha = 0.5 \text{ ps}^2$. The orange line is a fit for the lower envelope of the MOSAIC signal in order to obtain α .

3.7. Measurements and discussion

In order to determine the chirp of a laser pulse which only passed the pulse shaper as shown in figure 1.1, it was sent to the IAC. Afterwards, a signal was measured where an additional pulse expander was inserted as discussed in section 3.4. The comparison between these two is shown in figure 3.10. Compared to the simulations in figure 3.6 it is visible that the IAC of the laser pulse without the pulse expander fits the expected shape well, while the one with the pulse expander does not. Possible reasons could be that the chirp is too high for the model used in the simulation to work or that the pulse expander introduces side effects not considered in the simulation.

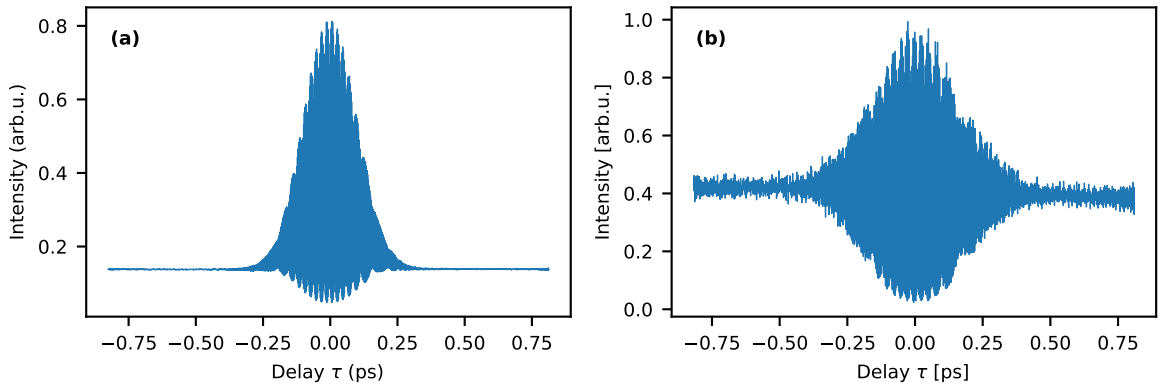


Figure 3.10.: Measured IAC of Ti:Sa Laser without (a) and with (b) pulse expander before the autocorrelator.

The same signals after applying the MOSAIC filter are shown in figure 3.11. It is visible that the lower envelopes in figure 3.11(a) and 3.11(b) do not resemble the expected ones in figure 3.7. As the laser signal without pulse expander was assumed to be relatively unchirped, it is already unexpected that the lower envelope differs that much from a constant line at zero intensity. One explanatory approach could be that the laser was already chirped to begin with. However, this would not explain why the shape of the lower envelope differs from the characteristic one of the simulation.

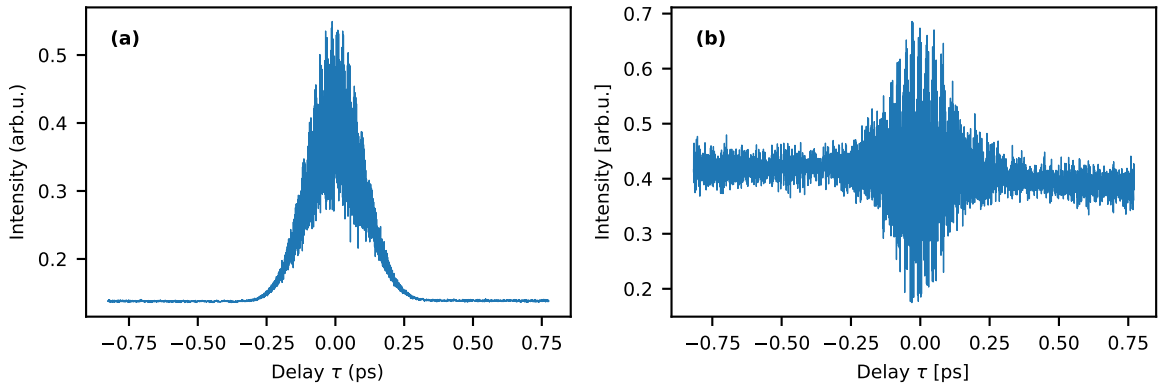


Figure 3.11.: Measured IAC of Ti:Sa Laser with applied MOSAIC filter without (a) and with (b) pulse expander before the autocorrelator.

4. Building up a scanning Fabry-Pérot interferometer from scratch

4.1. Introduction and motivation

The Fabry Pérot interferometer (FPI) is an optical resonator developed by Charles Fabry and Alfred Pérot. An incoming light beam will only be transmitted through the resonator consisting of two semi-transparent mirrors if it fulfils the resonance condition.[24]. The resonance frequencies can be changed by adjusting the mirror distance. By measuring the intensity at the output of the FPI, this can be used to resolve fine features of an electromagnetic spectrum, like e.g. the one of the exciton described in section 2.3. The following chapter introduces basics of electromagnetic radiation, describes simulations performed to size the components of the FPI and displays measurement techniques used to obtain the resolved exciton spectrum.

4.2. Transverse modes of electromagnetic radiation

4.2.1. Gaussian beam

In this chapter, light beams are described by the wave picture according to Meschede [25]. They fulfil the Maxwell equations and therefore their electric field $\mathbf{E}(\mathbf{r}, t)$ fulfils the wave equation

$$\left(\nabla^2 - \frac{1}{c^2} \frac{\partial^2}{\partial t^2} \right) \mathbf{E}(\mathbf{r}, t) = 0. \quad (4.1)$$

Along the propagation direction z a light beam behaves similarly to a plane wave with constant amplitude A_0 which is a known solution to the wave equation (4.1)

$$E(z, t) = A_0 e^{-i(\omega t - kz)}. \quad (4.2)$$

4. Building up a scanning Fabry-Pérot interferometer from scratch

However, far from its source light is expected to behave like a spherical wave

$$E(\mathbf{r}, t) = A_0 \frac{e^{-i(\omega t - \mathbf{k}\mathbf{r})}}{|\mathbf{k}\mathbf{r}|}. \quad (4.3)$$

To get a better understanding of the propagation of light, only paraxial (near the z-axis) parts of the spherical wave are considered. Additionally, the wave is split into its longitudinal (z-axis) part and its transversal part and beams with axial symmetry are assumed, which only depend on a transversal coordinate ρ . Under these circumstances $\mathbf{k}\mathbf{r}$ can be replaced with kr and because of $\rho \ll r, z$ the Fresnel approximation can be applied:

$$E(\mathbf{r}) = \frac{A(\mathbf{r})}{|\mathbf{k}\mathbf{r}|} e^{i\mathbf{k}\mathbf{r}} \simeq \frac{A(z, \rho)}{kz} \exp\left(i \frac{k\rho^2}{2z}\right) e^{ikz} \quad (4.4)$$

with $r = \sqrt{z^2 + \rho^2} \simeq z + \rho^2/2z$.

Equation (4.4) resembles the plain wave in equation (4.2), with the spacial phase transversal modulated by $\exp(ik\rho^2/2z)$. Another spherical wave solution can be obtained by applying the following replacement (z_0 is a real number)

$$z \rightarrow q(z) = z - iz_0. \quad (4.5)$$

Thereby, the fundamental (or TEM₀₀) Gaussian mode has been constructed

$$E(z, \rho) \simeq \frac{A_0}{kq(z)} \exp\left(i \frac{k\rho^2}{2q(z)}\right) e^{ikz}. \quad (4.6)$$

The electric and magnetic fields of Gauss modes are transversal to its propagation direction. These waveforms are called transversal electric and magnetic modes with indices (m, n) . Its fundamental solution is the TEM₀₀-Mode, which is the most important one and will therefore be examined in more detail in the rest of this subsection.

By executing the replacement $q(z) \rightarrow z - iz_0$ explicitly the equation (4.6) can be expressed as

$$\frac{1}{q(z)} = \frac{z + iz_0}{z^2 + z_0^2} = \frac{1}{R(z)} + i \frac{2}{k\omega^2(z)}, \quad (4.7)$$

with new variables z_0 , $R(z)$ and $\omega(z)$ being introduced. With the decomposition of the Fresnel factors into real and imaginary part, two factors can be identified: one complex phase factor, which describes the curvature of the wavefronts and a real factor, which describes the envelope of the beam. Therefore, the exponential in equation (4.6) becomes

$$\exp\left(i \frac{k\rho^2}{2q(z)}\right) \rightarrow \exp\left(i \frac{k\rho^2}{2R(z)}\right) \exp\left(-\left(\frac{\rho}{\omega(z)}\right)^2\right) \quad (4.8)$$

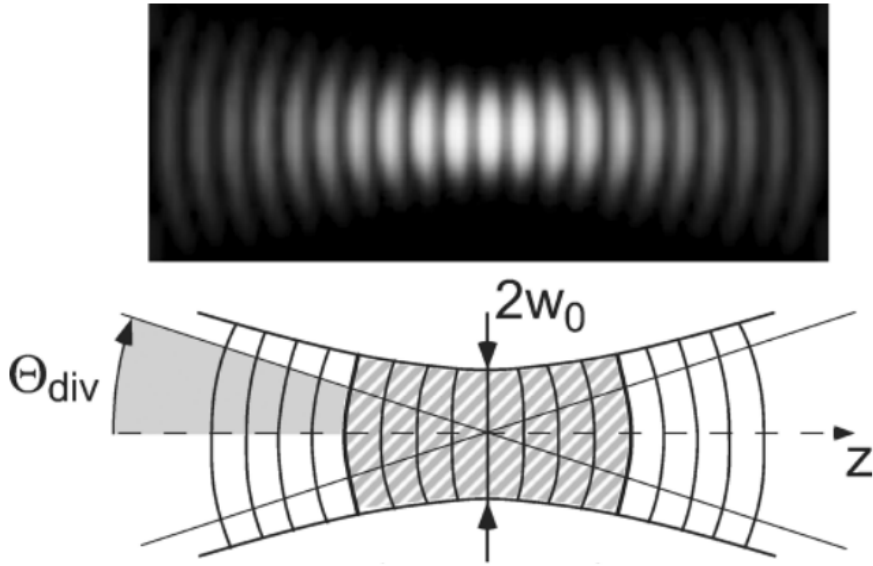


Figure 4.1.: A Gaussian beam near its beam waist. Near the center they resemble plan wave fronts, while outside they converge towards spherical wave fronts. They Rayleighzone is shaded at the lower part of the figure.[25]

For a proper description of a Gaussian beam as shown in figure 4.1 the following parameters have to be introduced

- **Evolving radius of curvature $R(z)$:**

$$R(z) = z(1 + (z_0/z)^2) \quad (4.9)$$

- **Beam waist $2\omega_0$:**

$$\omega_0^2 = \lambda z_0 / \pi \quad (4.10)$$

The beam waist $2\omega_0$ or beam radius ω_0 describes the smallest beam cross section at $z = 0$. If the wave propagates inside a medium with the refractive index n , λ has to be replaced with λ/n . The cross section of the beam waist is then $\omega_0^2 = \lambda z_0 / (\pi n)$.

A Gaussian beam can be completely characterized at every point z on the beam axis either with the parameter couple (ω_0, z_0) or alternatively with the real and imaginary part of $q(z)$. The parameters of the Gaussian beam are transformed by linear operations, which coefficients are identical to those from

geometrical optics

$$q_{out} = \frac{Aq_{in} + B}{Cq_{in} + D} \quad (4.11)$$

with the parameters A, B, C, D determined by the optical element transforming the Gaussian beam described by q_{in} .

4.2.2. Higher Gauss modes

The wave equation (4.1) can be simplified by only allowing monochromatic waves with harmonic time dependence

$$\mathbf{E}(\mathbf{r}, t) = \text{Re} \left(\mathbf{E}(\mathbf{r}) e^{-i\omega t} \right). \quad (4.12)$$

With $\omega^2 = c^2 \mathbf{k}^2$, the *Helmholtz equation* can be deduced, which only depends on the location \mathbf{r}

$$\left(\nabla^2 + \mathbf{k}^2 \right) \mathbf{E}(\mathbf{r}) = 0. \quad (4.13)$$

In favor of a formal treatment of the Gaussian modes, the Helmholtz equation is split into its transversal and longitudinal contributions,

$$\nabla^2 + k^2 = \frac{\partial^2}{\partial z^2} + \nabla_T^2 + k^2 \quad \text{with} \quad \nabla_T^2 = \frac{\partial}{\partial x^2} + \frac{\partial}{\partial y^2}. \quad (4.14)$$

Additionally, the electric field E of equation (4.4) is inserted into the Helmholtz equation. It is also assumed that the amplitude A only changes slowly in the order of the wavelength,

$$\frac{\partial}{\partial z} A = A' \ll kA, \quad (4.15)$$

which allows the approximation

$$\frac{\partial^2}{\partial z^2} A e^{ik\rho^2/(2z)} \frac{e^{ikz}}{kz} \simeq (2ikA' - k^2 A) e^{ik\rho^2/(2z)} \frac{e^{ikz}}{kz}, \quad (4.16)$$

and results in the *paraxial Helmholtz equation*,

$$\left(\nabla_T^2 + 2ik \frac{\partial}{\partial z} \right) A(\rho, z) = 0. \quad (4.17)$$

The fundamental solution is the TEM₀₀ mode in equation (4.6). Examples of higher modes can be found in figure 4.2.

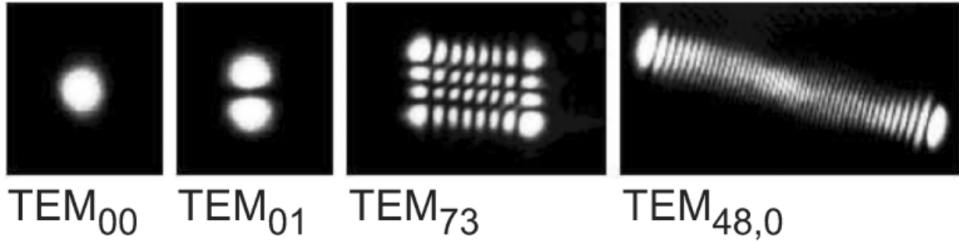


Figure 4.2.: Gaussian modes higher order of a simple Ti-sapphire laser. The asymmetry of the high modes are caused by technical inaccuracies of the resonator elements (mirrors, laser crystal).

4.3. Fundamentals of Fabry-Pérot interferometers

4.3.1. Resonator losses

For the following discussion of the FPI, a two-mirror-resonator with the reflecting surfaces facing each other and air as medium in between is assumed. The theoretical foundation is provided by the work of Ismail et al. [26].

The time the light needs for one roundtrip is given by

$$t_{RT} = \frac{2l}{c} \quad (4.18)$$

where l is the geometrical length of the resonator and c is the speed of light in air.

The photon-decay time τ_c of the interferometer is then given by

$$\frac{1}{\tau_c} = -\frac{\ln(R_1 \cdot R_2)}{t_{RT}} \quad (4.19)$$

where R_1 and R_2 are the corresponding intensity reflectivities of the mirrors.

The number of photons at frequency ν inside the resonator is described by the differential rate equation

$$\frac{d}{dt} \varphi(t) = -\frac{1}{\tau_c} \varphi(t). \quad (4.20)$$

With a number φ_s of photons at $t = 0$ the integration gives

$$\varphi(t) = \varphi_s e^{-t/\tau_c} \quad (4.21)$$

4.3.2. Resonance frequencies, free spectral range and spectral line shapes

The round-trip phase shift at frequency ν is given by

$$2\phi(\nu) = 2\pi\nu t_{RT} = 2\pi\nu \frac{2l}{c} \quad (4.22)$$

where $\phi(\nu)$ is the single-pass phase shift between the mirrors.

Resonances are visible for frequencies ν at which the light interferes constructively after one round trip. Two adjacent resonance frequencies differ in their round trip phase shift by 2π . Hence, the free spectral range $\Delta\nu_{FSR}$, the frequency difference between two adjacent resonance frequencies, can be calculated from equation (4.22)

$$2\Delta\phi_{FSR} = 2\pi \quad (4.23)$$

$$\Rightarrow 2\pi\Delta\nu_{FSR} \frac{2l}{c} = 2\pi \quad (4.24)$$

$$\Rightarrow \Delta\nu_{FSR} = \frac{c}{2l} \quad (4.25)$$

According to equation (4.21) the number of photons decays with the photon-decay time τ_c . With $E_{q,s}$ representing the initial amplitude, the electric field at ν_q is given by

$$E_q(t) = \begin{cases} E_{q,s} \cdot e^{i2\pi\nu_q t} \cdot e^{-t/(2\tau_c)} & t \geq 0 \\ 0 & t < 0 \end{cases}. \quad (4.26)$$

The Fourier transformation of the electric field can be expressed as

$$\tilde{E}_q(\nu) = \int_{-\infty}^{\infty} E_q(t) e^{-i2\pi\nu t} dt = E_{q,s} \int_0^{\infty} e^{[1/(2\tau_c) + i2\pi(\nu - \nu_q)]t} dt = E_{q,s} \frac{1}{(2\tau_c)^{-1} + i2\pi(\nu - \nu_q)}. \quad (4.27)$$

The normalized spectral line shape per unit frequency is then given by

$$\tilde{\gamma}_q(\nu) = \frac{1}{\tau_c} \left| \frac{\tilde{E}_q(\nu)}{E_{q,s}} \right|^2 = \frac{1}{\tau_c} \left| \frac{1}{(2\tau_c)^{-1} + i2\pi(\nu - \nu_q)} \right|^2 = \frac{1}{\tau_c} \frac{1}{(2\tau_c)^{-2} + 4\pi^2(\nu - \nu_q)^2} \quad (4.28)$$

$$= \frac{1}{\pi} \frac{1/(4\pi\tau_c)}{1/(4\pi\tau_c)^2 + (\nu - \nu_q)^2} \quad (4.29)$$

with $\int \tilde{\gamma}_q(\nu) d\nu = 1$.

By defining the full-width-at-half-maximum linewidth (FWHM) $\Delta\nu_c$, $\tilde{\gamma}_q(\nu)$ can be obtained

$$\Delta\nu_c = \frac{1}{2\pi\tau_c} \Rightarrow \tilde{\gamma}_q(\nu) = \frac{1}{\pi} \frac{\Delta\nu_c/2}{(\Delta\nu_c/2)^2 + (\nu - \nu_q)^2}. \quad (4.30)$$

Afterwards the Lorentzian lines are normalized so that the peak is at unity

$$\gamma_{q,L}(\nu) = \frac{\pi}{2} \Delta\nu_c \tilde{\gamma}_q(\nu) = \frac{(\Delta\nu_c)^2}{(\Delta\nu_c)^2 + 4(\nu - \nu_q)^2} \quad (4.31)$$

with $\gamma_{q,L}(\nu_q) = 1$.

4.3.3. Airy distribution of Fabry-Pérot interferometers

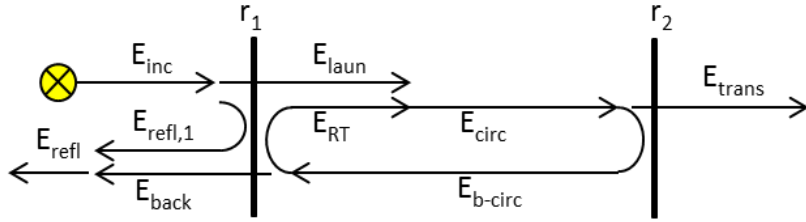


Figure 4.3.: FPI with electric field mirror reflectivities r_1 and r_2 . Indicated in this figure are the electric fields resulting from an incoming E_{inc} , the reflected field $E_{refl,1}$ and transmitted field E_{laun} . E_{circ} and $E_{circ,b}$ circulate inside the resonator, resulting in E_{RT} after one round-trip. E_{back} is the backwards transmitted field.[27]

The response of the FPI is calculated with the circulating-field approach [26], where a steady-state is assumed. E_{circ} is the result of E_{laun} interfering with E_{RT} . E_{laun} is the transmission of the incoming light E_{inc} and E_{RT} is E_{circ} after one round-trip in the resonator, i.e., after the outcoupling losses of mirror 1 and 2. Therefore, the field E_{circ} can be calculated from E_{laun} by

$$E_{circ} = E_{laun} + E_{RT} = E_{laun} + r_1 r_2 e^{-i2\phi} E_{circ} \Rightarrow \frac{E_{circ}}{E_{laun}} = \frac{1}{1 - r_1 r_2 e^{-i2\phi}} \quad (4.32)$$

where r_1 and r_2 are the electric-field reflectivities of mirror 1 and 2.

The generic Airy distribution only considers light inside the mirrors and is defined as

$$A_{circ} = \frac{I_{circ}}{I_{laun}} = \frac{|E_{circ}|^2}{|E_{laun}|^2} = \frac{1}{|1 - r_1 r_2 e^{-i2\phi}|^2} = \frac{1}{(1 - \sqrt{R_1 R_2})^2 + 4\sqrt{R_1 R_2} \sin^2(\phi)} \quad (4.33)$$

by using

$$\begin{aligned} |1 - r_1 r_2 e^{-i2\phi}|^2 &= |1 - r_1 r_2 \cos(2\phi) + i r_1 r_2 \sin(2\phi)|^2 = [1 - r_1 r_2 \cos(2\phi)]^2 + r_1^2 r_2^2 \sin^2(2\phi) \\ &= 1 + R_1 R_2 - 2\sqrt{R_1 R_2} \cos(2\phi) = (1 - \sqrt{R_1 R_2})^2 + 4\sqrt{R_1 R_2} \sin^2(\phi) \end{aligned}$$

and additionally $R_i = r_i^2$ and $\cos(2\phi) = 1 - 2\sin^2(\phi)$.

4. Building up a scanning Fabry-Pérot interferometer from scratch

Commonly, light is sent through the FPI. Therefore the following sections will use the Airy distribution A'_{trans} described by

$$A'_{trans} = \frac{I_{trans}}{I_{inc}} = \frac{I_{circ} \cdot (1 - R_2)}{I_{laun} / (1 - R_1)} = (1 - R_1)(1 - R_2) A_{circ} = \frac{(1 - R_1)(1 - R_2)}{(1 - \sqrt{R_1 R_2})^2 + 4\sqrt{R_1 R_2} \sin^2(\phi)} \quad (4.34)$$

with $\phi = \frac{\pi v}{\Delta\nu_{FSR}}$.

A'_{trans} is displayed in figure 4.4 for $R_1 = R_2$. The peak value at one of its resonance frequencies calculates as follows

$$A'_{trans} = \frac{(1 - R_1)(1 - R_2)}{(1 - \sqrt{R_1 R_2})^2} \stackrel{R_1=R_2}{=} 1. \quad (4.35)$$

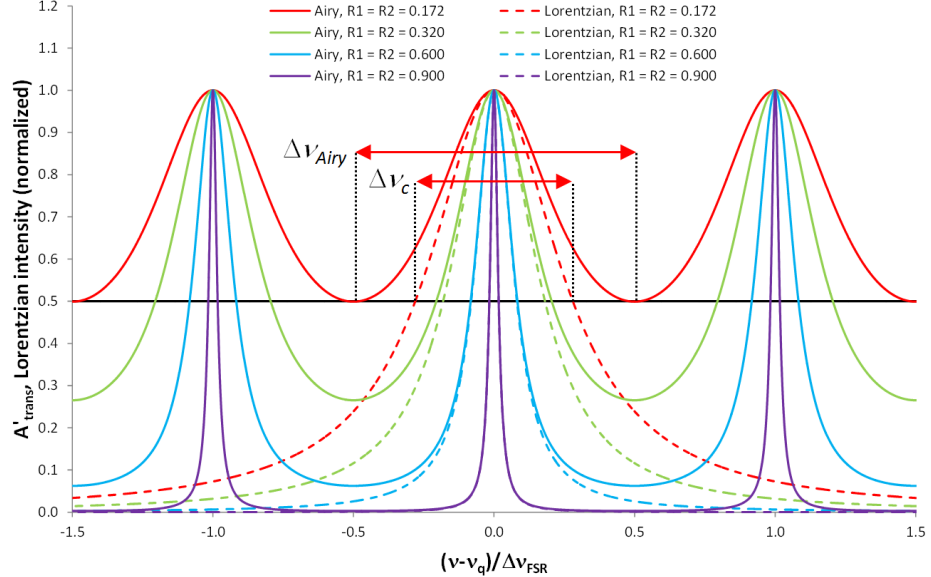


Figure 4.4.: Airy distribution A'_{trans} as described in equation (4.34) compared to the Lorentzian lines $\gamma_{q,L}$ as described in equation (4.31) [27].

4.3.4. Airy linewidth and finesse

The airy linewidth is defined as the full width at half maximum (FWHM) of A'_{trans} . It can be set in relation with the free spectral range $\Delta\nu_{FSR}$ and the mirror reflectivities as follows.

A'_{trans} decreases to half of its peak value at $A'_{trans}(v_q)/2$ when the phase shift ϕ changes by the amount

$\Delta\phi$ so that the denominator of A'_{trans} in equation (4.34) is twice as big

$$\left(1 - \sqrt{R_1 R_2}\right)^2 = 4\sqrt{R_1 R_2} \sin^2(\Delta\phi) \quad (4.36)$$

$$\Rightarrow \Delta\phi = \arcsin\left(\frac{1 - \sqrt{R_1 R_2}}{2\sqrt[4]{R_1 R_2}}\right) \quad (4.37)$$

With equation (4.22) and (4.25), the phase shift can be expressed as

$$\phi = \frac{\pi\nu}{\Delta\nu_{FSR}} \quad (4.38)$$

$$\Rightarrow \Delta\phi = \frac{\pi(\Delta\nu_{Airy}/2)}{\Delta\nu_{FSR}}. \quad (4.39)$$

Therefore, with equation (4.37) and (4.39) the FWHM linewidth is given by

$$\Delta\nu_{Airy} = \Delta\nu_{FSR} \frac{2}{\pi} \arcsin\left(\frac{1 - \sqrt{R_1 R_2}}{2\sqrt[4]{R_1 R_2}}\right). \quad (4.40)$$

The finesse of the Airy distribution of a FPI is defined as

$$F_{Airy} := \frac{\Delta\nu_{FSR}}{\Delta\nu_{Airy}} = \frac{\pi}{2} \left[\arcsin\left(\frac{1 - \sqrt{R_1 R_2}}{2\sqrt[4]{R_1 R_2}}\right) \right]^{-1} \quad (4.41)$$

and is therefore only dependent on the mirror reflectivities R_1 and R_2 .

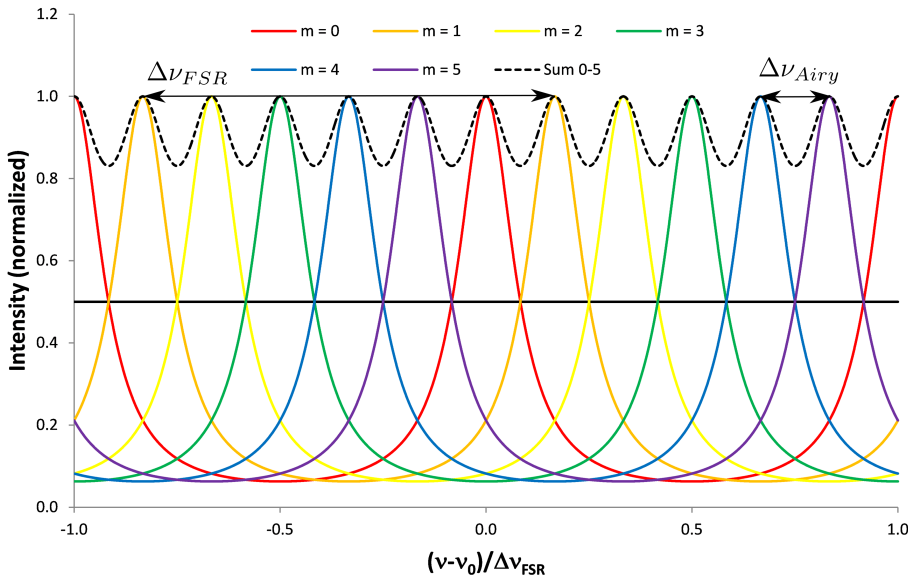


Figure 4.5.: Demonstration of the physical meaning of the Airy finesse F_{Airy} . The coloured lines are Airy distributions created by light at distinct frequencies ν_m , while scanning the resonator length. When the light occurs at frequencies $\nu_m = \nu_q + m\Delta\nu_{Airy}$, the adjacent Airy distributions are separated from each other by ν_{Airy} , therefore fulfilling the Taylor criterion. Since in this example $F_{Airy} = 6$ exactly six peaks fit inside the free spectral range. As can be seen in the figure the Airy finesse F_{Airy} quantifies the maximum number of peaks that can be resolved [27].

4. Building up a scanning Fabry-Pérot interferometer from scratch

The Airy finesse is the determining property when it comes to the spectral resolution of the FPI. This can be made visible by comparing its message with the Taylor criterion for the resolution of two adjacent peaks. The Taylor criterion proposes that two spectral lines are resolvable when the separation of the maxima is greater than the FWHM. As displayed in figure 4.5, the Airy finesse is equal to the number of Airy distributions originating from light at certain frequencies ν_m which do not overlap at a point higher than half of their maxima. Hence, the Airy finesse describes the spectral resolution in a way that is consistent with the Taylor criterion.

4.3.5. Mode matching and spatial filtering

One fundamental challenge of Fabry Pérot interferometry is how to efficiently couple an incident beam of light into a given mode of the resonator. The following discussion is based on the work of Yariv, Yeh, and Yariv [28] and Meschede [25].

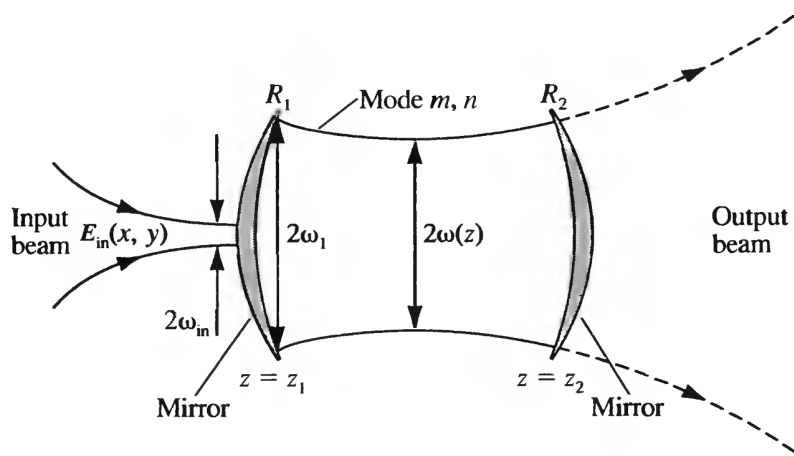


Figure 4.6.: Incident monochromatic beam of light exciting transverse mode m, n of a resonator [28]

In sketched with figure 4.6, an input beam E_{in} propagates into the resonator and potentially excite its modes $E_{mn}(x, y)$, where m, n are the transverse mode integers of the Gaussian beam of the optical resonator. Since $E_{mn}(x, y)$ describes a complete orthogonal set of wavefunctions they satisfy

$$\iint E_{mn}(x, y) E_{m'n'}^*(x, y) dx dy = 0 \quad \text{unless } m = m' \text{ and } n = n'. \quad (4.42)$$

and

$$E_{in}(x, y) = \sum_{mn} a_{mn} E_{mn}(x, y) \quad (4.43)$$

where a_{mn} are constants. By multiplying both sides of equation (4.43) with E_{mn}^* , integrating over the whole x - y -plane and using equation (4.42), the following expression can be obtained

$$a_{mn} = \frac{\iint E_{in}(x,y)E_{mn}^*(x,y)dxdy}{\iint E_{mn}(x,y)E_{mn}^*(x,y)dxdy} \quad (4.44)$$

The efficiency of coupling an incident field into a spatial mode E_{mn} is defined as

$$\eta_{mn} = \frac{\text{Power coupled into mode } mn}{\text{Total incident power}} = \frac{\iint |a_{mn}E_{mn}(x,y)|^2 dxdy}{\iint |E_{in}(x,y)|^2 dxdy}. \quad (4.45)$$

By inserting equation (4.44) into equation (4.45) the following expression can be obtained

$$\eta_{mn} = \frac{|\iint E_{in}(x,y)E_{mn}^*(x,y)dxdy|^2}{\iint |E_{in}(x,y)|^2 dxdy \cdot \iint |E_{mn}(x,y)|^2 dxdy}. \quad (4.46)$$

From equation (4.46) can be deduced that for an input beam with the *same* spatial dependency as the mode to be excited

$$E_{in}(x,y) \sim E_{mn}(x,y) \quad (4.47)$$

all of the incident power goes into E_{mn} , i.e. $\eta_{mn} = 1$ and all other $\eta_{m'n'}$ are zero. Usually, the fundamental TEM₀₀ mode is desired and equation (4.46) implies that a pure Gaussian beam excites only the fundamental mode and the interferometer will then irradiate a pure Gaussian beam as well. In practise, additional measures are necessary such as matching the radius of curvature by Gaussian beam focusing.

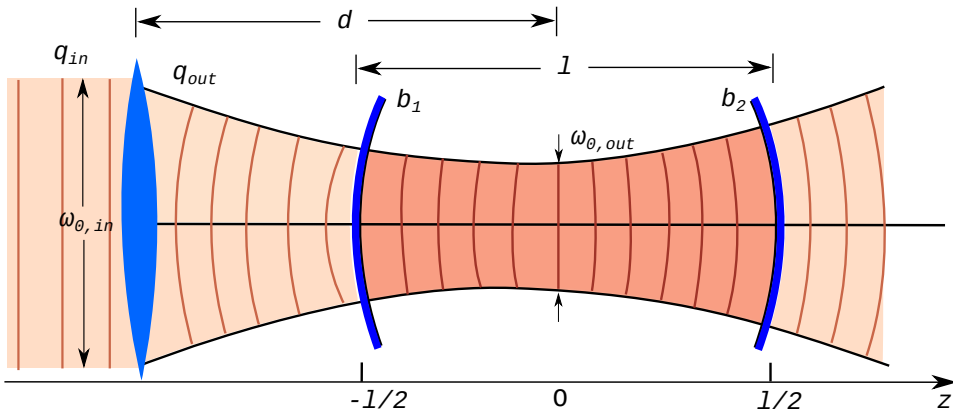


Figure 4.7.: Mode matching of an Gaussian beam into a Fabry Pérot interferometer. Incoming Gaussian beam described by q_{in} transformed by a lens into a Gaussian beam described by q_{out} . The parameters b_1 and b_2 describe the radii of the two mirrors.

In order to match the radius of curvature of the incoming Gaussian beam with the radius of curvature of the resonator a lens is inserted as depicted in figure 4.7. Light with a beam waist of ω_{01} gets focused

4. Building up a scanning Fabry-Pérot interferometer from scratch

into the resonator. Transformations by thin lenses can be described with the ABCD-rule introduced in subsection 4.2.1:

$$\begin{pmatrix} A & B \\ C & D \end{pmatrix} = \begin{pmatrix} 1 & 0 \\ \frac{-1}{f} & 1 \end{pmatrix} \quad (4.48)$$

with f as the wavelength of the lens. The incoming beam described by q_{in} is transformed by the lens into a beam described by q_{out} according to equation (4.10) and (4.11)

$$q_{in} = z + i \frac{\pi n \omega_{0,in}^2}{\lambda} \quad \text{and} \quad q_{out} = \frac{q_{in}}{q_{in} \cdot \frac{-1}{f} + 1} = z + i \frac{\pi n \omega_{0,out}^2}{\lambda} \quad (4.49)$$

with $n \approx 1$ for air. Together with equation (4.10) the following relation can be deduced

$$\omega_{0,out}^2 = \frac{\omega_{0,in}^2}{\left(1 - \frac{z}{f}\right)^2 + \left(\frac{\pi \omega_{0,in}}{\lambda f}\right)^2}. \quad (4.50)$$

The radii of curvature have to match. For given mirrors (described by R_{mirror}) and lens (described by f) the input beam waist has to be adjusted according to equation (4.9) and (4.10)

$$R_{mirror} \stackrel{!}{=} R_{gauss}(z = l/2) \quad (4.51)$$

$$R_{mirror} \stackrel{!}{=} \frac{l}{2} \left(1 + \left(\frac{2z_{0,out}}{l}\right)^2\right) \quad (4.52)$$

$$R_{mirror} \stackrel{!}{=} \frac{l}{2} \left(1 + \left(\frac{2\omega_{0,out}^2 \pi}{l \lambda}\right)^2\right). \quad (4.53)$$

Inserting equation (4.53) into equation (4.50) results in the condition for mode matching

$$R_{mirror} = \frac{l}{2} \left(1 + \left(\frac{\frac{2\omega_{0,in}^2 \pi}{l \lambda}}{\left(\left(1 - \frac{z}{f}\right)^2 + \left(\frac{\pi \omega_{0,in}}{\lambda f}\right)^2\right) l \lambda}\right)^2\right). \quad (4.54)$$

One way to further suppress higher modes is *spatial filtering*. It can be seen in figure 4.2 that the effective area of a mode increases with its order (m, n). Figure 4.8 shows one way to suppress higher modes consisting of a focusing lens and a pin hole which diameter matches the one of the TEM₀₀ mode.

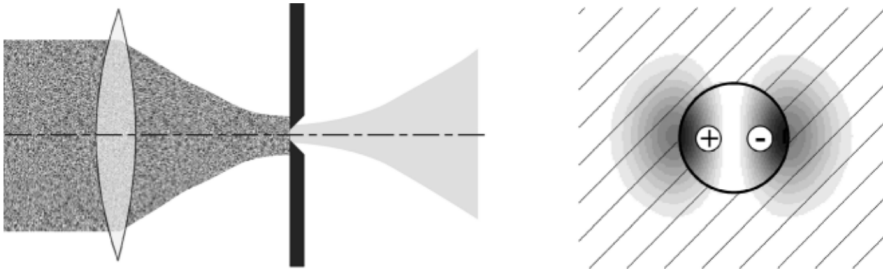


Figure 4.8.: Spatial filtering of Gauss modes. In front of the aperture, the beam consists of a superposition of multiple Gauss modes. In the example of TEM₀₁ is displayed how higher modes are suppressed by the aperture. [25]

4.3.6. Confocal setup

If the incoming beam would represent a perfect TEM₀₀ mode, spatial filtering would not be necessary and mode matching would not have to be done as precise. Unfortunately, this can not always be guaranteed and counteractions like mode matching and spatial filtering discussed in subsection 4.3.5 are tedious and error prone. Arranging the mirrors of an FPI into a confocal arrangement reduces the need for these measures. By giving up the ability to choose different free spectral ranges with a given pair of mirrors, the confocal setup liberates from mode matching considerations as the cavity is mode degenerated, i.e. the frequency of certain axial and transverse cavity modes are the same. The following discussion is based on the work of Hercher [29].

A quasi-monochromatic beam of wavelength λ_0 is composed of transverse modes TEM_{mnq}, where the subscripts m and n denote the amplitude distribution of the normal mode on a surface of constant phase and q the number of axial modes inside the resonator. Each of these modes resonates for mirror separations satisfying

$$l = \frac{\lambda_0}{2} \{ q + (1 + m + n) \cos^{-1} [(1 - l/b_1)(1 - l/b_2)]^{1/2} \} \quad (4.55)$$

where the parameters b_1 and b_2 describe the radii of the two mirrors as can be seen in figure 4.7.

For the confocal setup $l = b_1 = b_2$ justifies the approximation

$$l \approx \frac{\lambda_0}{2} [q + (1 + m + n)]. \quad (4.56)$$

The modes resonate at mirror separations of either

$$l = \frac{\lambda_0}{2}(p+1) \quad p \in \mathbb{N} \text{ and } (m+n) \text{ even}, \quad (4.57)$$

$$l = \frac{\lambda_0}{2}(p) \quad p \in \mathbb{N} \text{ and } (m+n) \text{ odd}. \quad (4.58)$$

If mode matching is not executed, it can be assumed that the incoming beam consists of an approximately equal number of even and odd transverse modes. The resonance cavity length l does not depend on n, m and q anymore but only on one integer p . The transversal modes are degenerate and fulfil

$$l = \frac{\lambda_0 p}{2}. \quad (4.59)$$

It can be additionally concluded from equation (4.59) that a change of $\lambda_0/2$ in the mirror separation scans through one free spectral range.

4.4. Simulation

The goal in building up a scanning FPI is to resolve features of the emission spectra of GaAs quantum dots described in chapter 2. More precisely, it is intended to resolve the shape of the ZPL and the PSB. Equation 4.41 shows that the finesse is constant for a given pair of mirrors. If the spectrum to be resolved is broad, a higher free spectral range $\Delta\nu_{FSR}$ has to be chosen, under the loss of resolution. If the spectrum contains fine details which need to be resolved, a lower ν_{Airy} has to be chosen, which results in a lower free spectral range $\Delta\nu_{FSR}$. Hence, the thin ZPL and the broad PSB can not be resolved with the same setup. Instead, the mirror distances have to be adjusted and in the confocal setup discussed in subsection 4.3.6 the mirrors have to be changed as well.

The zero-phonon line is described with a Cauchy distribution

$$\Phi_{dot,zero}(\lambda) = \frac{1}{\pi \cdot \Delta\lambda_{zero} \cdot 0.5 \left[1 + \left(\frac{\lambda - \lambda_{0,zero}}{\Delta\lambda_{zero} \cdot 0.5} \right)^2 \right]} \quad (4.60)$$

with $\lambda_{0,zero}$ as the center wavelength and $\Delta\lambda_{zero}$ as the spectral range of the zero-phonon line which can be found in table 2.1.

The phonon side band is described with a Gauss distribution

$$\Phi_{dot,side}(\lambda) = \frac{1}{\sqrt{2 \cdot \pi \cdot \Delta\lambda_{side}^2}} \cdot \exp \left(-\frac{(\lambda - \lambda_{0,side})^2}{2 \cdot \Delta\lambda_{side}^2} \right) \quad (4.61)$$

with $\lambda_{0,side}$ as the center wavelength and $\Delta\lambda_{side}$ as the spectral range of the phonon side band which can be found in table 2.1 as well.

Together they describe the excitonic emission of the QD

$$\Phi_{dot}(\lambda) = \Phi_{dot,zero}(\lambda) + \Phi_{dot,phonon}(\lambda) \quad (4.62)$$

depicted in figure 4.9.

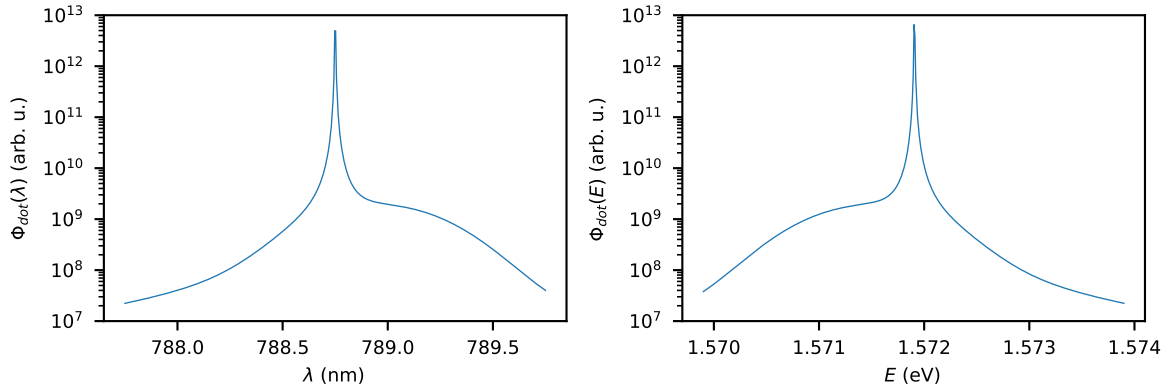


Figure 4.9.: Simulated exciton emission of a GaAs quantum dot plotted dependant on the wavelength λ and the Energy E . The parameters can be found in table 2.1.

$\Phi_{dot}(E)$ is transmitted through the FPI. As discussed the mirror distance l is adjusted to a value which depends if a resolved ZPL or a resolved PSB is desired. A comparison of the FPI transmission $A'_{trans}(E)$ described in equation 4.34 with $R_1 = R_2 = 98\%$ and $\Phi_{dot}(E)$ is shown in figure 4.10.

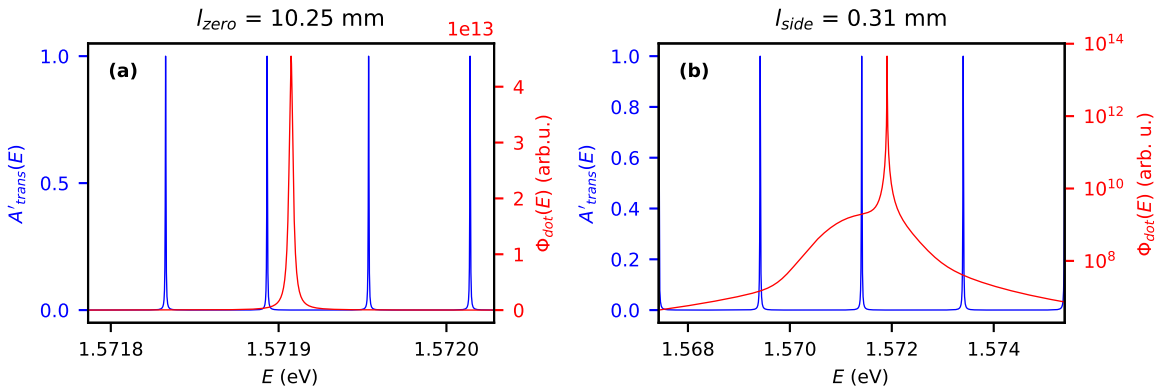


Figure 4.10.: Transmission of the FPI modes A'_{trans} compared to the exciton emission $\Phi_{dot}(E)$ for (a) ZPL and (b) PSB.

4. Building up a scanning Fabry-Pérot interferometer from scratch

The FPI scans by continuously varying the mirror distance l with a certain stepsize Δl and measuring the output-photon-flux every time. This process is sketched in figure 4.11.

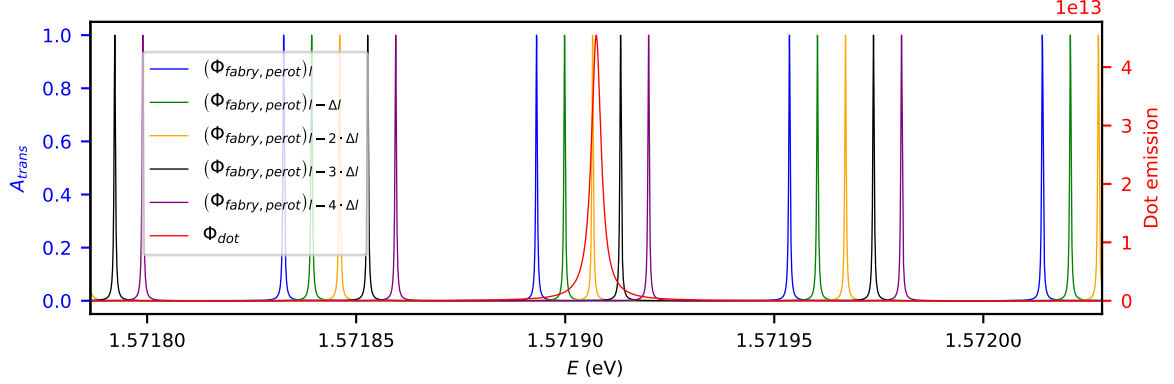


Figure 4.11.: Transmissions of the FPI modes A'_{trans} for different mirror distances $l - m \cdot \Delta l$ with $m \in \mathbb{N}$ compared to the exciton emission $\Phi_{dot}(E)$.

The output-photon-flux of the scanning FPI is then described with the convolution of $\Phi_{dot}(E)$ and $A'_{trans}(E)$

$$\Phi_{fabry,perot,unnormalized}(\nu) = \int_{\nu_0 - \Delta\nu_{FSR} \cdot n_{peaks}^{0.5}}^{\nu_0 + \Delta\nu_{FSR} \cdot n_{peaks}^{0.5}} \Phi_{dot}(\nu') A'_{trans}(\nu - \nu') d\nu' \quad (4.63)$$

with ν_0 as the central frequency of the exciton emission line and $n_{peaks} = 4$ as the number of airy peaks considered for the numerical convolution.

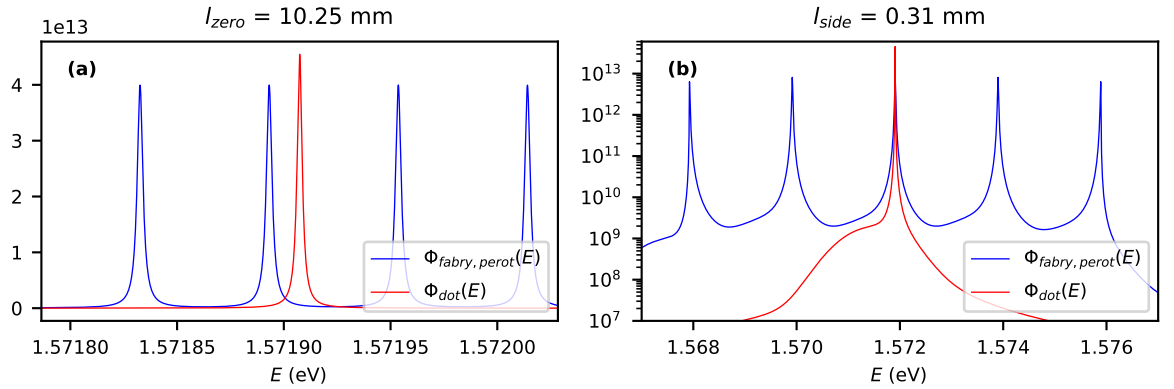


Figure 4.12.: Output-photon-flux of the scanning FPI $\Phi_{fabry,perot}(E)$ compared to the exciton emission $\Phi_{dot}(E)$ for (a) ZPI and (b) PSB.

$\Phi_{fabry,perot,unnormalized}(\nu)$ can then be normalized with the integral of $A'_{trans}(\nu)$ over the same range

$$\Phi_{fabry,perot}(\nu) = \frac{\Phi_{fabry,perot,unnormalized}(\nu)}{\int_{\nu_0 - \Delta\nu_{FSR}/0.5}^{\nu_0 + \Delta\nu_{FSR}/0.5} A'_{trans}(\nu) d\nu} \quad (4.64)$$

A comparison of $\Phi_{fabry,perot}(E)$ and $\Phi_{dot}(E)$ is shown in figure 4.12.

From now on, only the ZPL-path is shown as no new information is gained by examining both. In order to estimate the accuracy of the scanning FPI, one of the FPI modes is shifted in order to overlap with $\Phi_{fabry,perot}(E)$ as depicted in figure 4.13(a). Afterwards, the absolute difference between those two $|\Phi_{dot}(E) - \Phi_{fabry,perot}(E)|$ is calculated as shown in figure 4.13(b). Now the relative error of $\Phi_{fabry,perot}(E)$ for the given parameters and compared to the actual excitonic QD emission can be calculated

$$\epsilon_{fabry,perot} = \frac{\int_{\nu_0 - \Delta\nu_{FSR}/0.5}^{\nu_0 + \Delta\nu_{FSR}/0.5} |\Phi_{fabry,perot,shifted}(\nu) - \Phi_{dot}(\nu)| d\nu}{\int_{\nu_0 - \Delta\nu_{FSR}/0.5}^{\nu_0 + \Delta\nu_{FSR}/0.5} \Phi_{dot}(\nu) d\nu} \quad (4.65)$$

For the parameters in the ZPL path this gives $\epsilon_{fabry,perot,ZPL} = 10.57\%$.

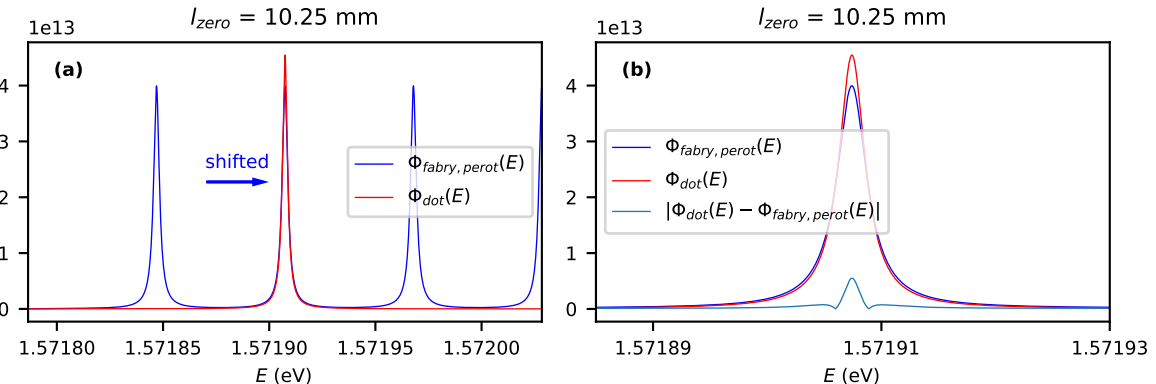


Figure 4.13.: Output-photon-flux of the scanning FPI $\Phi_{fabry,perot}(E)$ compared to the exciton emission $\Phi_{dot}(E)$. In (a) $\Phi_{fabry,perot}(E)$ is $\Phi_{dot}(E)$, then in (b) the absolute difference $|\Phi_{fabry,perot,shifted}(\nu) - \Phi_{dot}(\nu)|$ is displayed $|\Phi_{fabry,perot}(\nu) - \Phi_{dot}(\nu)|$.

4.5. Setup

Multiple FPI setups were built up in order to test their suitability to resolve QD emission. The first version featured planar mirrors, while their distance was coarsely tunable with an adjustable platform and finely tunable with a piezoelectrical actuator. However this setup with planar mirrors proved to be highly unstable and was therefore discarded. The second version used smaller, planar-convex mirrors and a ground plate made of molybdenum. This resulted in a stable FPI which was also adjustable for various free-spectral ranges. The measurements discussed in section 4.6 are obtained with this setup. However, the effort needed to mode-match for every measurement is too large to actually use it in further experiments. That is why the confocal setup will be used in the future, even though the freedom to adjust the free-spectral range is lost.

In order to obtain the spectral emission of the input signal, the FPI is used in the scanning mode. Here one of the mirrors is attached to a piezoelectric actuator which moves the mirror stepwise after every measurement as shown in figure 4.14. A minimal sketch of the setup is visible in figure 1.1.

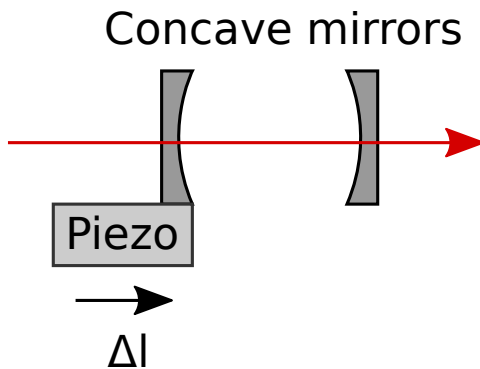


Figure 4.14.: Scanning Fabry Pérot interferometer

4.5.1. Live avalanche photodiode mode

Before the scanning FPI can be used to measure QD emission, it has to be aligned first. As every sweep with the charge-coupled devices (CCDs) takes time in the order of minutes, avalanche photodiodes (APDs) were used. A function generator is used to drive the piezoelectrical actuator and the Hydra Harp correlates the measurements of the APD with the TTL-output of the function generator. The complete setup is sketched in figure 4.15.

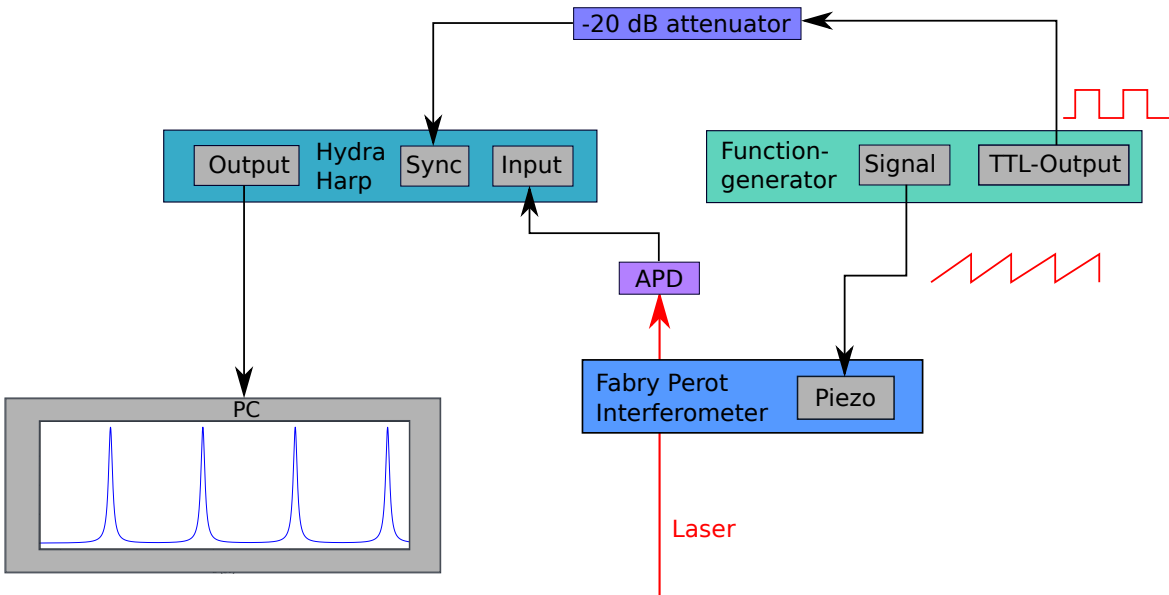


Figure 4.15.: Live avalanche photodiode setup

4.6. Measurements and discussion

In the following measurements the FPI was set up in the non-confocal mode and HeNe laser signals were used in order to align it. This involves for one setting the mirrors coming before the FPI so that the laser beam goes straight and centred through the FPI mirrors and then setting the FPI mirrors so that they are parallel and a single laser beam emerges as is shown in figure 4.16.

4. Building up a scanning Fabry-Pérot interferometer from scratch

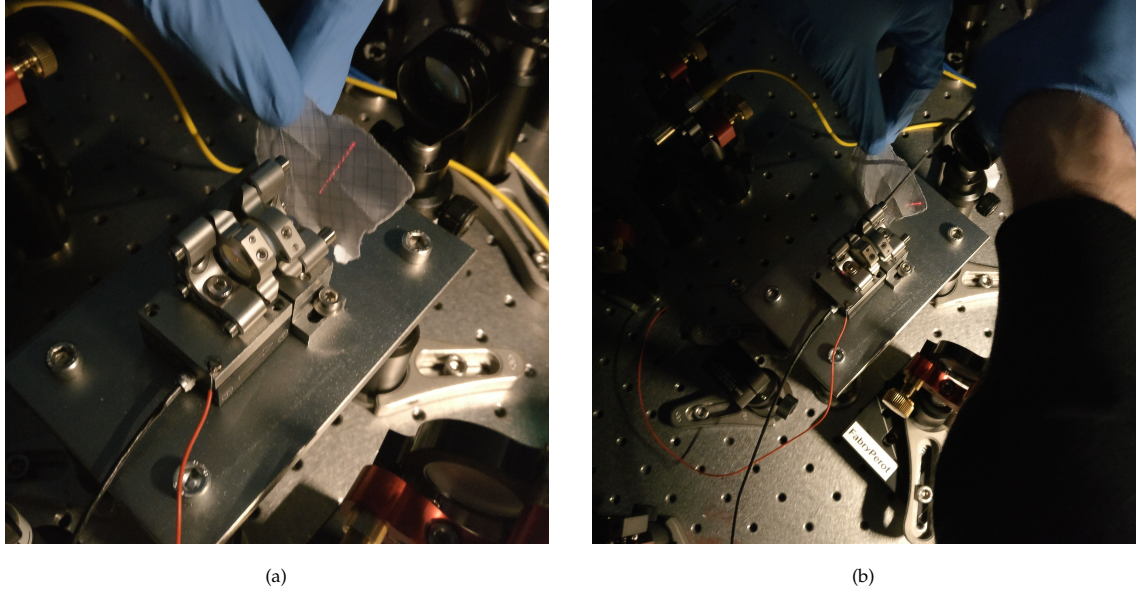


Figure 4.16.: Aligning the Fabry Pérot interferometer

Without spatial restriction strong TEM-modes of higher order are visible in figure 4.17(a). To counteract, a pinhole is inserted and adjusted which results in the measurement visible in figure 4.17(b).

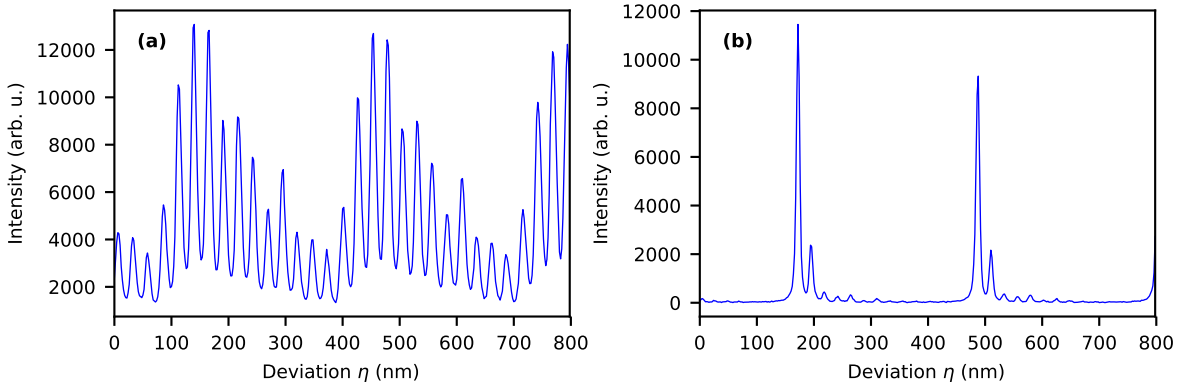


Figure 4.17.: Transmission measurement of FPI with ground mirror distance $l \approx 2$ mm and HeNe laser. (a) was aligned without spatial filtering with a pinhole and (b) involved a pinhole.

Set up like this, the GaAs QD sample AS2o8 was measured. First a polarization map of the exciton was recorded in order to determine the FSS $E_{FSS} = 24.42(39)$ μeV with the data shown in figure 4.18.

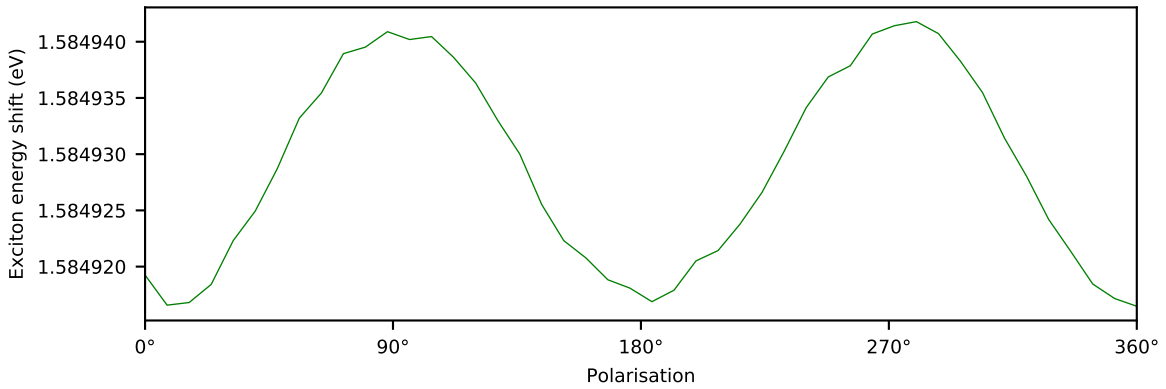


Figure 4.18.: Polarization map of exciton of QD in sample AS208.

Afterwards the output of the QD through the FPI was measured while the mirror distance was stepwisely changed which is shown in figure 4.19. The x-scale on the top of figure 4.19 was calculated by correlating the distance between the two adjacent peaks with the FSS determined with the data of figure 4.18. For this QD results in a conversion between the deviations $\eta = 1 \text{ nm} \hat{=} \zeta = 1.19(2) \mu\text{eV}$.

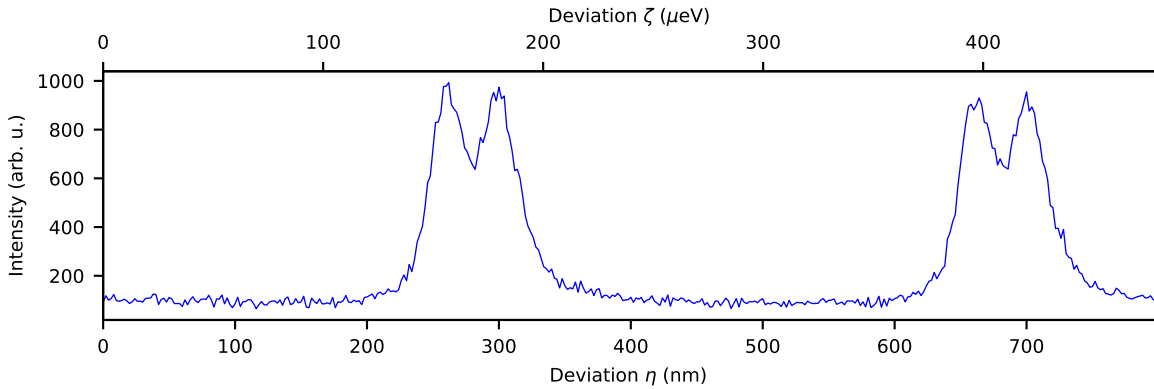


Figure 4.19.: Finestructure measurement of biexciton of QD in sample AS208 by passing thorough FPI and sweeping the mirror distance. Ground mirror distance was $l \approx 2 \text{ mm}$.

5. Summary and outlook

The first topic presented in this thesis is entangled photon generation using ARP with frequency-chirped-pulses. The obstacles in quantifying the chirp just with IAC were discussed and one possible solution (MOSAIC) was presented. Finally, the pulse expander, used for deterministically adjusting the chirp, was introduced and measurements with and without the pulse expander were presented. However, the Ti:Sa laser used for these experiments later turned out to be heavily chirped to begin with, which made comparisons difficult. Additionally, it had to be sent away for reparation, which blocked further investigations. The next steps will be to investigate MOSAIC under different scenarios and then, if the chirp can be adjusted, attempt to excite the GaAs QDs via ARP.

The second topic presented is the build-up of a scanning FPI from scratch. After setting up the theoretical foundation of electromagnetic waves and different FPI setups, simulations were presented in order to determine component parameters suitable for the wanted FPI mode properties. Afterwards, measurements were presented, which involved aligning the FPI with a HeNe laser, mode matching and spatial filtering. Finally, measurements of the FSS of a GaAs QD were presented and evaluated in order to confirm the consistency between the measured and the simulated results for the free spectral range. The next steps will be to set up the FPI in the confocal mode and measure with it the FSS as well. It might be advisable to buy multiple sets of mirrors in order to fulfil different needs regarding spectral width and resolution. When this is accomplished the scanning FPI can be used as "black box", which comes into action whenever fine details of QD emission need to be resolved.

Appendix

Appendix A.

Acronyms

QKD	quantum key distribution	1
QD	quantum dot	1
MBE	molecular beam epitaxy	3
CB	conduction band	3
VB	valence band	3
X	exciton	4
XX	biexciton	4
ZPL	zero phonon line	6
PSB	phonon side band	6
HBT	Hanbury-Brown-Twiss	11
BS	beam splitter	11
ARP	adiabatic rapid passage	13
IAC	interferometric autocorrelation	15
MOSAIC	modified-spectrum autointerferometric correlation	16
FPI	Fabry P��rot interferometer	23
FWHM	full width at half maximum	30
APD	avalanche photodiode	41
CCD	charge-coupled device	41
FSS	fine structure splitting	1

Bibliography

- [1] Jonathan P. Dowling and Gerard J. Milburn. "Quantum technology: the second quantum revolution." In: *Philosophical Transactions of the Royal Society of London. Series A: Mathematical, Physical and Engineering Sciences* 361.1809 (Aug. 15, 2003). Ed. by A. G. J. MacFarlane, pp. 1655–1674. ISSN: 1471-2962. DOI: 10.1098/rsta.2003.1227. URL: <http://www.royalsocietypublishing.org/doi/10.1098/rsta.2003.1227> (visited on 07/08/2019) (cit. on p. 1).
- [2] M. Bayer et al. "Fine structure of neutral and charged excitons in self-assembled In(Ga)As/(Al)GaAs quantum dots." In: *Physical Review B* 65.19 (May 7, 2002). ISSN: 0163-1829, 1095-3795. DOI: 10.1103/PhysRevB.65.195315. URL: <https://link.aps.org/doi/10.1103/PhysRevB.65.195315> (visited on 06/17/2019) (cit. on pp. 1, 6).
- [3] Johannes D Plumhof et al. "Experimental methods of post-growth tuning of the excitonic fine structure splitting in semiconductor quantum dots." In: *Nanoscale Research Letters* 7.1 (Dec. 2012). ISSN: 1556-276X. DOI: 10.1186/1556-276X-7-336. URL: <https://nanoscalereslett.springeropen.com/articles/10.1186/1556-276X-7-336> (visited on 07/01/2019) (cit. on p. 1).
- [4] Harishankar Jayakumar et al. "Deterministic Photon Pairs and Coherent Optical Control of a Single Quantum Dot." In: *Physical Review Letters* 110.13 (Mar. 26, 2013). ISSN: 0031-9007, 1079-7114. DOI: 10.1103/PhysRevLett.110.135505. URL: <https://link.aps.org/doi/10.1103/PhysRevLett.110.135505> (visited on 06/18/2019) (cit. on p. 1).
- [5] Christian Schimpf. "Towards quantum teleportation with remote quantum dots." PhD thesis. 2017 (cit. on pp. 2, 5, 9, 11, 12).
- [6] Daniel Huber. "GaAs quantum dots: A Dephasing-Free Source of Entangled Photon Pairs." PhD thesis. 2019 (cit. on pp. 3–5, 9–11).
- [7] Zh. M. Wang et al. "Nanoholes fabricated by self-assembled gallium nanodrill on GaAs(100)." In: *Applied Physics Letters* 90.11 (Mar. 12, 2007), p. 113120. ISSN: 0003-6951, 1077-3118. DOI: 10.1063/1.2713745. URL: <http://aip.scitation.org/doi/10.1063/1.2713745> (visited on 06/13/2019) (cit. on p. 3).

Bibliography

- [8] R. M. Stevenson et al. "A semiconductor source of triggered entangled photon pairs." In: *Nature* 439.7073 (Jan. 2006), pp. 179–182. ISSN: 0028-0836, 1476-4687. DOI: 10.1038/nature04446. URL: <http://www.nature.com/articles/nature04446> (visited on 06/17/2019) (cit. on p. 4).
- [9] E. Peter et al. "Phonon sidebands in exciton and biexciton emission from single GaAs quantum dots." In: *Physical Review B* 69.4 (Jan. 26, 2004), p. 041307. ISSN: 1098-0121, 1550-235X. DOI: 10.1103/PhysRevB.69.041307. URL: <https://link.aps.org/doi/10.1103/PhysRevB.69.041307> (visited on 06/11/2019) (cit. on p. 6).
- [10] Josef Friedrich and Dietrich Haarer. "Photochemical Hole Burning: A Spectroscopic Study of Relaxation Processes in Polymers and Glasses." In: *Angewandte Chemie International Edition in English* 23.2 (Feb. 1984), pp. 113–140. ISSN: 0570-0833, 1521-3773. DOI: 10.1002/anie.198401131. URL: <http://doi.wiley.com/10.1002/anie.198401131> (visited on 06/11/2019) (cit. on p. 6).
- [11] *Zero-phonon line and phonon sideband - Wikipedia*. URL: https://en.wikipedia.org/wiki/Zero-phonon_line_and_phonon_sideband (visited on 06/11/2019) (cit. on p. 7).
- [12] Eva Schöll et al. "Resonance fluorescence of GaAs quantum dots with near-unity photon indistinguishability." In: *Nano Letters* 19.4 (Apr. 10, 2019), pp. 2404–2410. ISSN: 1530-6984, 1530-6992. DOI: 10.1021/acs.nanolett.8b05132. arXiv: 1901.09721. URL: <http://arxiv.org/abs/1901.09721> (visited on 05/09/2019) (cit. on pp. 8, 9).
- [13] Takashi Kuroda et al. "Symmetric quantum dots as efficient sources of highly entangled photons: Violation of Bell's inequality without spectral and temporal filtering." In: *Physical Review B* 88.4 (July 18, 2013). ISSN: 1098-0121, 1550-235X. DOI: 10.1103/PhysRevB.88.041306. URL: <https://link.aps.org/doi/10.1103/PhysRevB.88.041306> (visited on 06/18/2019) (cit. on p. 9).
- [14] Peter Michler, ed. *Single semiconductor quantum dots*. Nanoscience and technology. OCLC: ocn248993461. Berlin: Springer, 2009. 389 pp. ISBN: 978-3-540-87445-4 978-3-540-87446-1 (cit. on p. 9).
- [15] S. Stufler et al. "Two-photon Rabi oscillations in a single In_xGa_{1-x}AsGaAs quantum dot." In: *Physical Review B* 73.12 (Mar. 7, 2006). ISSN: 1098-0121, 1550-235X. DOI: 10.1103/PhysRevB.73.125304. URL: <https://link.aps.org/doi/10.1103/PhysRevB.73.125304> (visited on 06/19/2019) (cit. on p. 10).
- [16] Marcus Reindl et al. "Phonon-Assisted Two-Photon Interference from Remote Quantum Emitters." In: *Nano Letters* 17.7 (July 12, 2017), pp. 4090–4095. ISSN: 1530-6984, 1530-6992. DOI: 10.1021/acs.nanolett.7b00777. URL: <http://pubs.acs.org/doi/10.1021/acs.nanolett.7b00777> (visited on 06/19/2019) (cit. on p. 10).

- [17] J. Förstner et al. "Phonon-Assisted Damping of Rabi Oscillations in Semiconductor Quantum Dots." In: *Physical Review Letters* 91.12 (Sept. 16, 2003). ISSN: 0031-9007, 1079-7114. DOI: 10.1103/PhysRevLett.91.127401. URL: <https://link.aps.org/doi/10.1103/PhysRevLett.91.127401> (visited on 06/19/2019) (cit. on p. 10).
- [18] M. Glässl et al. "Biexciton state preparation in a quantum dot via adiabatic rapid passage: Comparison between two control protocols and impact of phonon-induced dephasing." In: *Physical Review B* 87.8 (Feb. 8, 2013). ISSN: 1098-0121, 1550-235X. DOI: 10.1103/PhysRevB.87.085303. URL: <https://link.aps.org/doi/10.1103/PhysRevB.87.085303> (visited on 05/13/2019) (cit. on pp. 14, 17, 18).
- [19] Toshiyuki Hirayama and Mansoor Sheik-Bahae. "Real-time chirp diagnostic for ultrashort laser pulses." In: *Optics Letters* 27.10 (May 15, 2002), p. 860. ISSN: 0146-9592, 1539-4794. DOI: 10.1364/OL.27.000860. URL: <https://www.osapublishing.org/abstract.cfm?URI=ol-27-10-860> (visited on 05/13/2019) (cit. on pp. 14, 16).
- [20] *Optical autocorrelation - Wikipedia*. URL: https://en.wikipedia.org/wiki/Optical_autocorrelation (visited on 06/25/2019) (cit. on p. 16).
- [21] O. Martinez. "3000 times grating compressor with positive group velocity dispersion: Application to fiber compensation in 1.3-1.6 um region." In: *IEEE Journal of Quantum Electronics* 23.1 (Jan. 1987), pp. 59–64. ISSN: 0018-9197. DOI: 10.1109/JQE.1987.1073201. URL: <http://ieeexplore.ieee.org/document/1073201/> (visited on 06/28/2019) (cit. on pp. 16, 17).
- [22] H. Y. Hui and R. B. Liu. "Proposal for geometric generation of a biexciton in a quantum dot using a chirped pulse." In: *Physical Review B* 78.15 (Oct. 20, 2008). ISSN: 1098-0121, 1550-235X. DOI: 10.1103/PhysRevB.78.155315. URL: <https://link.aps.org/doi/10.1103/PhysRevB.78.155315> (visited on 06/24/2019) (cit. on p. 17).
- [23] Miles V. Klein and Thomas E. Furtak. *Optics*. 2nd ed. New York: Wiley, 1986. 660 pp. ISBN: 978-0-471-87297-9 (cit. on p. 20).
- [24] Timo Kaldewey et al. "Coherent and robust high-fidelity generation of a biexciton in a quantum dot by rapid adiabatic passage." In: *Physical Review B* 95.16 (Apr. 10, 2017). ISSN: 2469-9950, 2469-9969. DOI: 10.1103/PhysRevB.95.161302. arXiv: 1701.01371. URL: <http://arxiv.org/abs/1701.01371> (visited on 12/11/2018) (cit. on p. 23).
- [25] Dieter Meschede. *Optik, Licht und Laser*. 3., durchges. Aufl. Studium. OCLC: 254422596. Wiesbaden: Vieweg + Teubner, 2008. 568 pp. ISBN: 978-3-8351-0143-2 (cit. on pp. 23, 25, 32, 35).

Bibliography

- [26] Nur Ismail et al. "Fabry-Pérot resonator: spectral line shapes, generic and related Airy distributions, linewidths, finesse, and performance at low or frequency-dependent reflectivity." In: *Optics Express* 24.15 (July 25, 2016), p. 16366. ISSN: 1094-4087. DOI: 10.1364/OE.24.016366. URL: <https://www.osapublishing.org/abstract.cfm?URI=oe-24-15-16366> (visited on 05/13/2019) (cit. on pp. 27, 29).
- [27] *Fabry-Pérot interferometer - Wikipedia*. URL: https://en.wikipedia.org/wiki/Fabry%E2%80%93P%C3%A9rot_interferometer (visited on 05/06/2019) (cit. on pp. 29–31).
- [28] Amnon Yariv, Pochi Yeh, and Amnon Yariv. *Photonics: optical electronics in modern communications*. 6th ed. The Oxford series in electrical and computer engineering. OCLC: ocm58648003. New York: Oxford University Press, 2007. 836 pp. ISBN: 978-0-19-517946-0 (cit. on p. 32).
- [29] Michael Hercher. "The Spherical Mirror Fabry-Perot Interferometer." In: *Applied Optics* 7.5 (May 1, 1968), p. 951. ISSN: 0003-6935, 1539-4522. DOI: 10.1364/AO.7.000951. URL: <https://www.osapublishing.org/abstract.cfm?URI=ao-7-5-951> (visited on 05/09/2019) (cit. on p. 35).